805442

BOEING

SEATTLE, WASHINGTON

(6) AN EVALUATION OF THE RADIATION HAZARD DUE TO SOLAR-PARTICLE EVENTS,

(14) D2-90469

by

(10) W. R. Webber,* ~~Consultant to Space Physics Group Nuclear and Space Physics~~
J. R. Benbrooks, J. R. Thomas, Al Hunting, Richard Duncan

Second Printing

(11) December 1963 (13) 101 p.

Aero-Space Division
THE BOEING COMPANY
Seattle, Washington

*Professor of Physics, University of Minnesota

CONTENTS

CONTENTS (Cont'd)

LIST OF FIGURES

LIST OF FIGURES (Cont'd)

LIST OF TABLES

SUMMARY

This document contains a ~~concise but~~ comprehensive treatment of the current knowledge of solar-particle events.

A qualitative description has been given of the various methods of detecting solar-particle events, and all of the pertinent data available have been tabulated.

The characteristics of each of the events have been determined and from these, the intensities and the characteristic rigidities have been estimated for each event.

Based upon this information, the radiation doses have been calculated for each event and cumulative dose-probability curves have been derived.

Comments are included regarding missions in solar cycle 20 and various techniques for predicting the occurrences of solar-particle events.

ACKNOWLEDGEMENTS

This document was prepared under the supervision of Dr. W. R. Sheldon of the Space Physics Group, The Boeing Company, and is intended to supersede Boeing document D2-11608 entitled "Analysis of Solar-Flare Hazard to Manned Space System."

The section entitled "Solar-Particle Event Radiation Dose Determination" was prepared by J. R. Benbrook, Space Physics Group, The Boeing Company.

Other members of the Space Physics Group who assisted materially in the preparation are: J. R. Thomas, Al Hunting, and Richard Duncan.

INTRODUCTION

Although the characteristics of the galactic cosmic radiation have been recognized and investigated in detail for many years, the ability of the sun to produce large bursts of cosmic radiation has been studied in detail only since 1956. In the fifteen years preceding the great solar-cosmic-ray event of February 23, 1956, there were only four cases of an increase of cosmic-ray intensity at the earth (as measured at ground level by ionization-type detectors) that could be related to specific solar activity (Ref. 1). Therefore, the idea became widespread that these events were quite rare.

In the period subsequent to 1956, a wide variety of new techniques have been employed to advance our understanding of the solar-cosmic-ray events. These include particle counters and emulsions flown in balloons, satellites, and space probes, as well as measurements of reduction of cosmic noise caused by polar cap absorption (PCA).

With these techniques, studies of solar-particle bursts over the last few years are beginning to provide a reasonably complete picture of these events (Refs. 2, 3, and 4). The cosmic-ray particles ejected from the sun are known to be primarily protons with typically steep energy (or rigidity) spectra. Particle energies range from less than 10 Mev to a few Gev on occasion. Alpha particles and heavier nuclei, principally the C, N, O

group, may also be present in significant numbers.

These solar cosmic rays begin to arrive near the earth within minutes after they are produced in the region of a flare on the sun. The intensity of the solar cosmic rays is a strong function of solar activity. Such cosmic-ray particles are present near the earth in detectable numbers a significant fraction of the time (5 to 10 percent) and exceed the normal galactic-cosmic-ray intensity for a much smaller period (~1 percent). Occasionally, for intervals of one or two days, their intensities are many thousands of times greater than the galactic-cosmic-ray intensity. On the other hand, at periods near sunspot minimum, one to two years may elapse between significant solar-particle outbursts.

The intensity-time, directional, spectral, and charge characteristics of solar cosmic rays differ considerably from event to event. For example, most events have many more low energy particles than high energy ones. But some events, which produce a rare effect in a sea-level detector, contain a relatively large fraction of high-energy particles, correspondingly few low-energy particles, and thus give a small integrated particle intensity. This latter characteristic causes the event to be classified as a relatively small one. Other important dissimilarities exist from event to event and, for this reason, we shall catalog some of the more important ones individually.

In contrast to the solar cosmic rays, the galactic cosmic radiation

exhibits a rather regular behavior. It, too, consists primarily of protons with a significant admixture of alpha particles and heavier nuclei. The proportions of the various charge components remain constant throughout the cycle of solar activity while the total particle intensity changes by a factor of five. Maximum intensity of galactic cosmic rays occurs at sunspot minimum in anti-correlation with the solar activity. The spectrum changes only slowly during the course of the sunspot cycle. Near sunspot minimum there are more low-energy particles and, consequently, the spectrum is steeper. In fact, primarily the lower-energy particles (< 5 Gev) are affected as a result of the solar activity.

CHARACTERISTICS OF SOLAR-COSMIC-RAY EVENTS

Before considering some of the features of the production of solar cosmic rays, we shall establish some sort of workable picture of the characteristics of the solar-cosmic-ray events themselves. As we have pointed out, the details of each cosmic-ray event may differ considerably. Nevertheless, we may define certain general characteristics common to all events.

INTENSITY-TIME PROFILE

A typical event will have a set of intensity-time profiles, one for each energy, such as those shown in Fig. 1. Certain times characterize each profile.

Onset-Delay Time

The onset-delay time is defined as the time from the maximum intensity of the optical flare to the arrival of the first particles at the earth. This time is variable from event to event and is strongly energy-dependent, with the higher energies arriving first. It also depends on the location of the flare on the sun, with those on the west portion of the visible sun having shorter onset-delay times than those on the east portion. The onset-delay times may vary from a few minutes for high-energy particles (> 500 Mev) in some events

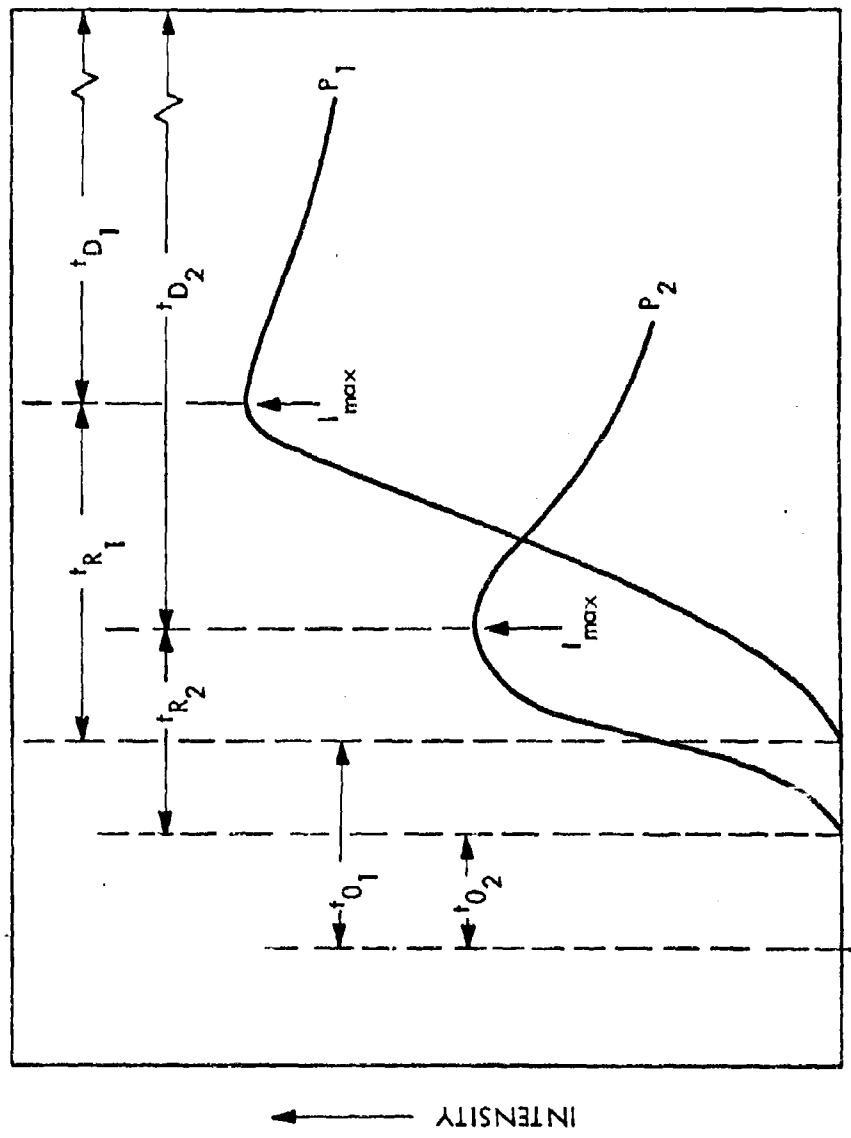

FIGURE 1. Typical intensity-time profiles for various rigidities in a solar-cosmic-ray event.

to many hours for low-energy particles (< 30 Mev) in other events.

Rise Time

The rise time is defined as the time interval at the earth from the first arrival of particles of a particular energy to the time at which the maximum intensity of these particles is attained. This time is strongly energy-dependent, for the higher energies reach maximum intensity first. There is evidence that this rise is exponential with time (Ref. 5) in a number of events. This allows us to define a characteristic rise time, t_R. This time is usually closely related to the onset-delay time in a particular event and depends in a similar manner on the location of the flare on the sun. The rise time may range from a few minutes for high-energy particles in some events occurring near the west limb of the sun to many hours for low-energy particles from events occurring near the east limb of the sun.

Decay Time

A growing body of evidence (Refs. 3 and 5) indicates that the decay of particles above a particular energy (or rigidity) is also exponential at most times and over a wide range of energies. Thus we may define a characteristic decay time, t_D, and write the following equation for the intensity of flare particles with energies greater than some energy, E, at some time, t, after the maximum intensity of particles, $I_{max}(E)$, is attained:

$$I = I_{max}(E) \exp(-t/t_D)$$

The time t_D, a function of energy, is smaller for higher energies. It is variable from event to event, although the variation seems to be influenced more by general interplanetary conditions than by the location of the flare, which governs the onset-delay and rise times. A sudden change in the interplanetary magnetic field configuration during the course of an event may drastically affect the decay rate, as measured by the decay time. In simple events, this time may range from two to four hours for high-energy particles to two to four days for low-energy particles. Generally, then, the decay time is longer than the rise time, in some instances up to ten times as long.

ANISOTROPIES IN SOLAR COSMIC RAYS

For the most part, the solar flare particles reach the vicinity of the earth very nearly isotropically (within ± 5 to 10 percent), and the aforementioned intensity-time characteristics refer to this isotropic radiation. However, significant anisotropies in the direction of arrival of solar-flare particles at the earth do exist. In particular, the particles appear to arrive from a highly preferred and fairly narrow direction 30° to 60° west of the earth-sun line (Ref. 6). This behavior is most pronounced for the high-energy particles. This directional radiation is usually of short duration

compared to the isotropic part, but intensities about 10 to 100 times the maximum isotropic radiation may occur in the preferred direction for a few minutes. As a result of the action of the geomagnetic field, this radiation approaches the surface of the earth in certain well-defined areas called impact zones.

ENERGY SPECTRUM OF FLARE PARTICLES

It is obvious from the foregoing discussion of the intensity-time characteristics of the flare particles and from the energy dependence of each of the parameters involved that the measured energy spectrum for any one event will depend upon the specific time during the event at which the measurements are made. The problem of determining a useful and meaningful representation of the solar flare particle spectrum has been one of the most difficult connected with the study of the flare particles. Usually, the differential number spectrum of the flare particles has been expressed either as a power-law energy spectrum, $dJ/dE = K_1/E^{n_1}$ or as a power-law rigidity spectrum, $dJ/dP = K_2/P^{n_2}$ (the rigidity of a particle = $P = pc/Ze$, where p is the particle momentum, c the velocity of light, e the unit charge, and Z the charge number of the particle). When either of these representations is used, n_1 (or n_2) is a function of both energy (or rigidity) and time. For example, n_1 (or n_2) is usually smaller for lower energies or rigidities because of the "bending over" of

the spectrum. Also, n_1 (or n_2) increases with time after the onset of an event, as the particle spectrum steepens with time.

Because the energy or rigidity interval viewed in any one measurement is usually quite narrow, it is possible to represent reasonably well the number spectrum of solar-flare particles as a power-law energy or rigidity spectrum with an n which is constant over the interval of measurement. This does not prove to be a useful representation over the entire range of rigidities involved in the solar outburst, however.

After a careful examination of the data from a large number of events, which were difficult to interpret if the solar-particle spectrum were considered to be a power law in either energy or rigidity, the conclusion has been reached that an exponential rigidity spectrum best describes the solar flare particles (Ref. 4). This spectrum is of the form $dJ/dP = dJ/dP_o \exp[-P/P_o(t)]$. The characteristic rigidity P_o in a specific event is a function of time only, and P_o decreases as the event progresses. Its value and time-dependence vary from event to event. Such spectra apply to all energies greater than 2 Mev if the time from the flare is a few times the onset-delay time for particles of a particular energy.

The time development of a typical solar-cosmic-ray spectrum during an event is shown in Fig. 2. Typical values of the characteristic

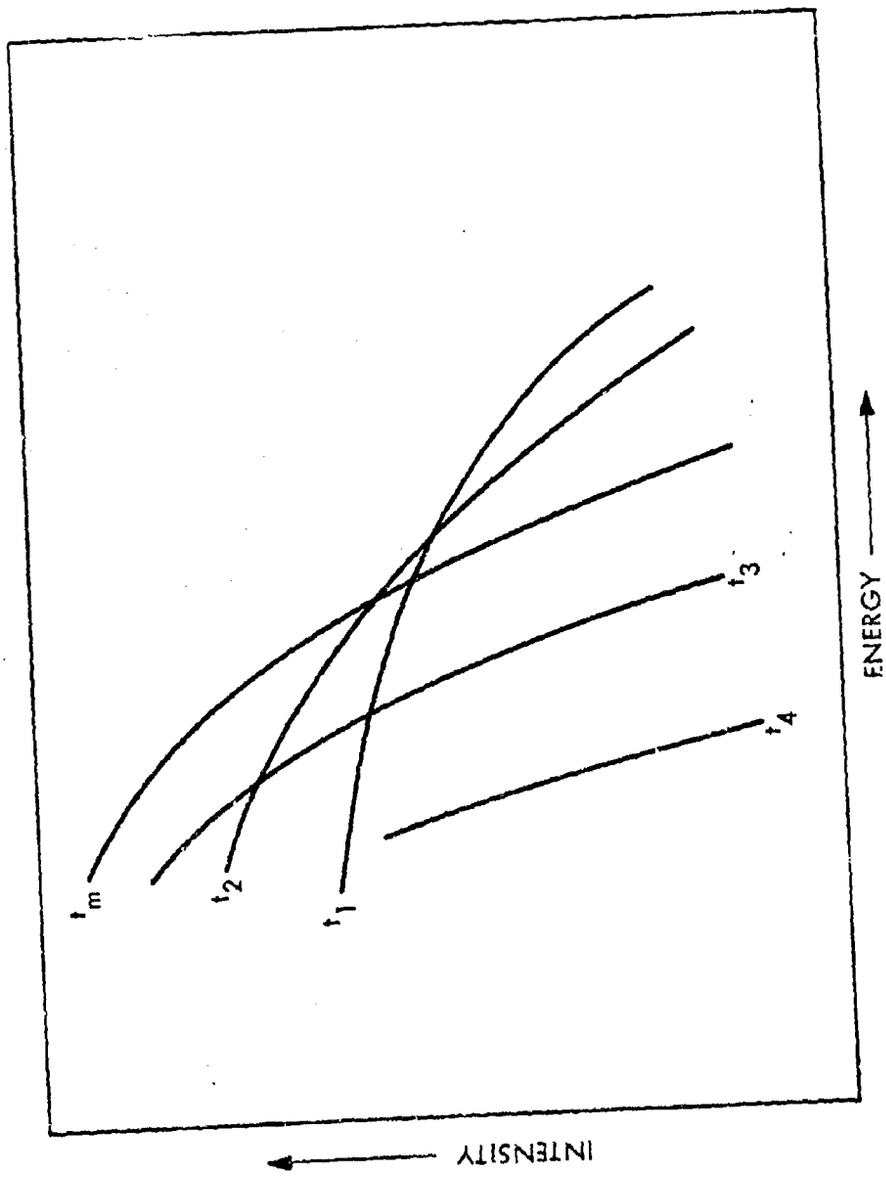

FIGURE 2. Typical energy spectra obtained at different times during a single event.

rigidity P_o, associated with times near the occurrence of I_{max} for the low-energy particles, may range from about 300 Mv in events with very flat spectra containing many high-energy particles to about 50 Mv in events with very steep spectra containing many low-energy particles and producing strong radio-wave absorption.

CHARGE COMPOSITION OF FLARE PARTICLES

Until recently, it was thought that the particles emitted in a solar flare burst were predominantly protons. Recent observations have established the presence of alpha particles in at least nine events and heavier particles (principally the M group consisting of carbon, oxygen, nitrogen and fluorine) in three events (Refs. 7 and 8). These heavier particles appear to have exponential rigidity spectra similar to the proton spectra. Thus, at any time the same P_o applies to protons, alphas, and heavier nuclei. The ratios of the values of J_o for each charge group (e.g., $J_{op}/J_{o\alpha}$, $J_{o\alpha}/J_{oM}$) are approximately constant during an event, although this ratio varies from event to event. Observations at rigidities greater than 0.5 Gv have revealed a $J_{op}/J_{o\alpha}$ that varies from one to about twenty with a predominance of values near one. The ratio $J_{o\alpha}/J_{oM}$, deduced from observations in the same rigidity range, appears to be a constant from event to event with a value approximately 60. Since all charge components appear to have similar rigidity spectra above ~ 0.5 Gv, and if this similarity continues to low

rigidities, then in events where $J_{op}/J_{o\alpha}$ is about one, we should expect equal total numbers of protons and alpha particles. The presence of these alpha particles has not been directly determined, but their presence may be inferred from radio-absorption measurements (Ref. 9).

If an alpha particle and a proton have the same range, then the alpha particle always has a greater rigidity, exactly double at non-relativistic energies. (Note that alphas and protons of the same range have the same energy per nucleon.) On this basis, we can account for the experimental observation of fewer alphas than the $J_{op}/J_{o\alpha}$ ratio predicts. The ratio of alphas to protons with a given range increases with decreasing range. Also, this ratio is a function of the characteristic P_o so that at ranges less than 1 gm/cm^2 and for flat spectra ($P_o > 100$ Mv), the ionization produced by alphas may dominate in the cases where $J_{op}/J_{o\alpha}$ is about one. The same considerations apply to the heavier nuclei (principally oxygen) so that the ionization produced by these particles can be a significant fraction (~50 percent) of that produced by protons at depths less than 1 gm/cm^2.

SOLAR FEATURES ASSOCIATED WITH COSMIC-RAY OUTBURSTS

It is clearly established that solar cosmic rays detected near the earth originate in connection with large flares on the visible disk of the sun. Flares are sudden increases in intensity of optical radiation over large areas in the solar atmosphere. The size scale for flares is based on their area, with the largest flares (3+) having an area greater than 1000×10^{-6} of the solar surface. Increases in the optical radiation, which occur principally in hydrogen line emission, e.g., H_α, form a negligible fraction of the over-all energy output of the sun. In addition, large increases in solar energy output occur at both ends of the electromagnetic spectrum: at wavelengths less 10 Å, corresponding to X rays and gamma rays, and at the radio end of the spectrum. Of particular interest in association with the cosmic-ray output are the radio emissions in the so-called microwave bursts at frequencies > 3000 Mc/s (wavelengths < 10 cm). These will be discussed later in greater detail.

A flare is not a separate or distinct event but originates in so-called active regions or centers on the sun. Therefore, the study of flares starts, in effect, with observations related to the life history of an active region. An active region first puts in its appearance as a small plage region located in one of the two sunspot belts, either north or south at a latitude of 5° to 40°. A few days later, sunspots appear in the region and proceed to grow

in number and in size as the size and brightness of the plage increases. Sunspots are cooler than the surrounding photosphere and have strong magnetic fields associated with them. The darker central region of a spot is called the umbra, and the gray region around it, the penumbra. As the spot group continues to grow, small flares occur and active bright filaments (or prominences) begin to appear. When the spot group reaches maximum size, the flares become larger and more numerous. At this stage of development, or somewhat later, cosmic-ray events are most likely to occur. This stage may be reached in three to four days in some instances, although typically the time is about thirty days.

The features associated with the cosmic-ray flares and their centers are very complex indeed; however, certain characteristics appear to stand out. These are described below.

CONNECTION WITH LARGE FLARES

Cosmic-ray events generally occur in connection with the larger solar flares. These flares have areas of bright emission which are comparable to the area of the entire associated sunspot group ($\sim 2000 \times 10^6$ of the solar hemisphere).

LARGE AND COMPLEX SPOT GROUPS

The spot group itself is generally large and complex with a complex magnetic field configuration. Also, a high level of flare activity and

frequent radio bursts are associated with the spot group.

H_α RADIATION

Those flares that produce cosmic rays are characterized by an unusual flash of radiation in H_α. It is believed that during this period of one to two minutes the cosmic rays are accelerated in the region of bright filaments that form over sunspot umbrae. Generally, there are two bright parallel filaments separated by the magnetic axis which is a line dividing the main North poles from the main South poles within the group (Ref. 10).

MICROWAVE RADIO EMISSION

The flares that produce cosmic rays are also characterized by microwave (cm) radio emission of exceptional intensity. This emission appears and disappears with a very rapid time scale of the same order as the optical emission. The source location is closely associated with the flare region; the height of the source, about 0.05 solar radii above the photosphere, is constant in time (Ref. 11). The source has roughly the same dimensions as the flare region. Undoubtedly, this emission is the radio analogue of the optical flash and is an essential accompaniment of the generation by these flares of relativistic particles. The close association between this portion of the radio emission and synchrotron emission of electrons moving in strong local fields is an interesting measure of the particle acceleration (Ref. 12).

METHODS OF DETECTING SOLAR COSMIC RAYS

In order to interpret solar-cosmic-ray events, we must understand, among other things, the methods used to detect these particles. Before discussing the cosmic-ray events themselves, then, we shall briefly discuss some of the detectors and their relative sensitivities.

NEUTRON MONITOR

The neutron monitor consists of a structure of BF_3 proportional counters surrounded by an arrangement of lead and paraffin. A high-energy (> 100 Mev) neutron or proton passing through the lead has a high probability of undergoing an interaction in which some of the reaction products are neutrons. These neutrons are slowed down in the paraffin by collisions with hydrogen nuclei and are then detected by the proportional counters. Since neutron monitors are usually located at or near sea level, the detected particles are, for the most part, the secondary nucleonic component of the primary radiation. The relation between this secondary radiation and the particles incident on the top of the atmosphere is a complicated function. It is the result of a nucleonic cascade and is best expressed in terms of a specific yield function. An example of the relative yield of secondaries at sea level as a function of rigidity of the primary particles at the top is shown (Ref. 13) in Fig. 3. It can be seen from

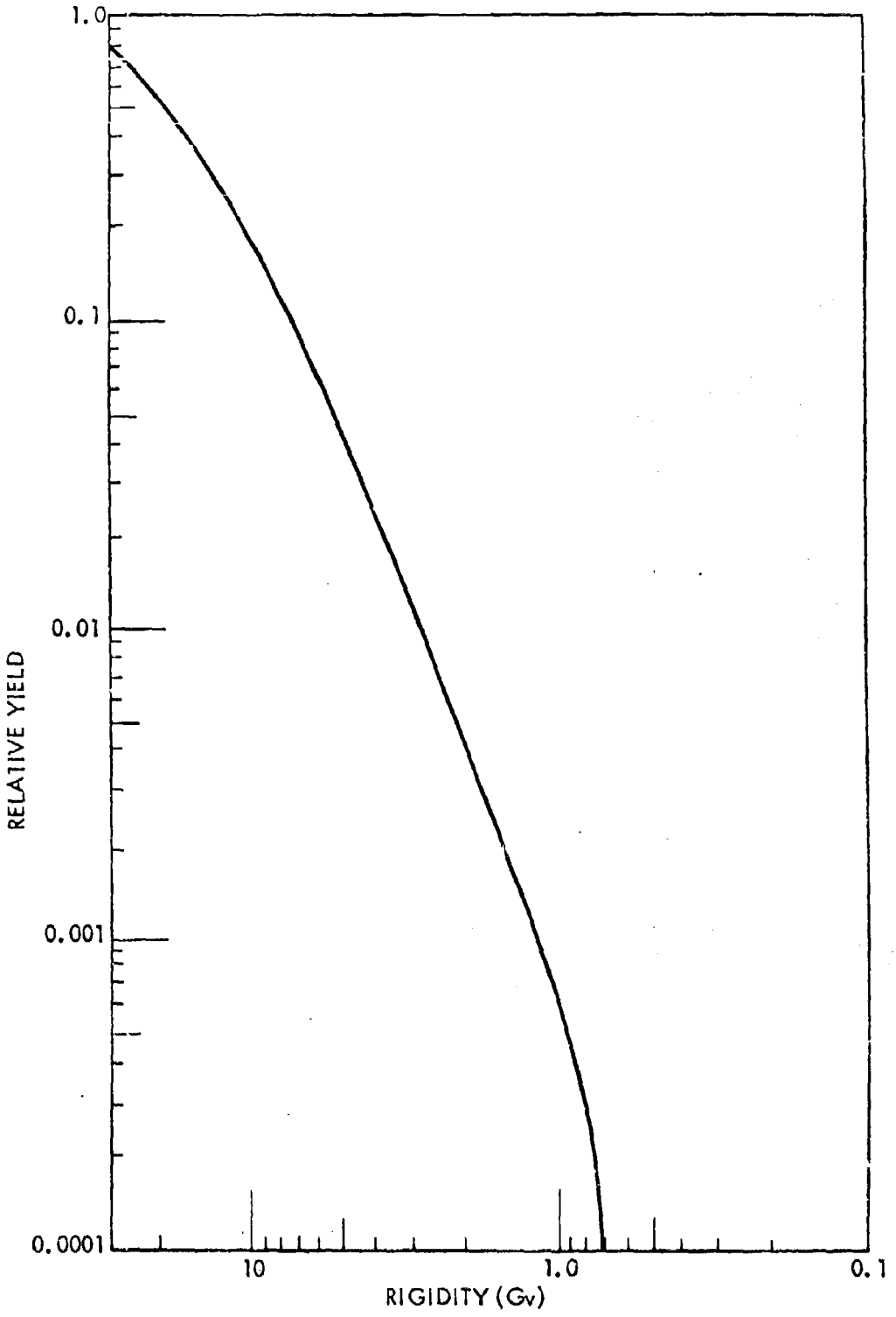

FIGURE 3. Yield function for neutron monitors.

this figure that the neutron monitor is relatively insensitive to the less-than-1-Gv-rigidity particles which form the main bulk in events with steep spectra. Only events where substantial numbers of particles above 1 Gv occur (P_o generally greater than 100 Mv) will be observed by these detectors operating near sea level.

DIRECT PRIMARY PARTICLE DETECTORS

The sensitivity to low-energy particles for this group of detectors is generally limited by two things: (1) the geomagnetic latitude at which the observation is made, and (2) the amount of air mass above the detector. The limitations on energy as a function of air mass and latitude are shown in Fig. 4. Since the essential form of all of these detectors can be carried on either a balloon, rocket, or satellite, the difference in sensitivity is mainly one of air mass or absorber. Here a rocket or satellite has a distinct advantage over a balloon. The balloon-borne detector, of course, has an overwhelming advantage over a neutron monitor at sea level in the detection of low-energy particles.

The types of detectors classified as direct particle detectors include the ones described below.

Geiger Counter

This device simply counts the total (integral) number of particles

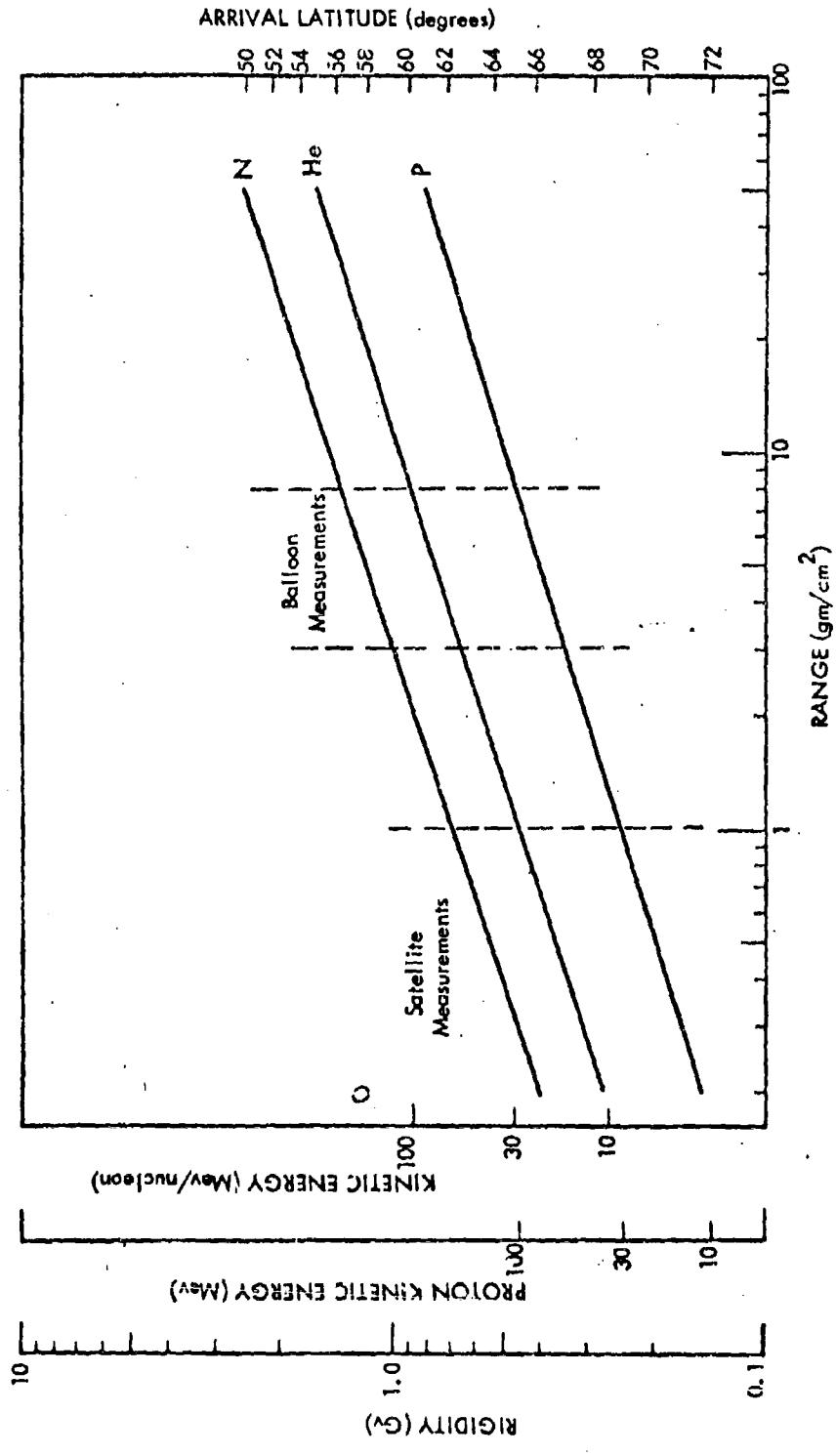

FIGURE 4. Relations between arrival latitude, range and energy for various cosmic-ray events.

passing through it. Since it always must observe solar cosmic rays relative to the background of galactic cosmic rays, this background sets the limit to the sensitivity. The geiger counter may be used to give time and direction discrimination and, with absorbers, crude energy measurements.

Ion Chamber

This device counts the total (integral) ionization of the particles passing through it. It also must observe the solar cosmic rays relative to the galactic-cosmic-ray background which sets the limit to its sensitivity. However, since the specific ionization of the solar particles is greater than that of the galactic ones, an ion chamber has a greater sensitivity than a comparable geiger counter. The ion chamber may be used to give time measurements, but direction and energy measurements using it alone have not been tried. It has been used to advantage in conjunction with a geiger counter to obtain energy-spectrum and charge-composition measurements of the solar particles.

Energy-Loss Measuring Devices

These devices, used individually, provide information similar to that obtained by using an ion chamber, but they may be readily combined in various ways for use in telescopes which measure directly the energy and charge of the particles passing through. Such detectors include scintillation and Cerenkov counters for acceptance-solid-angles (ASA) exceeding 1 cm^2

steradian and solid state detectors for ASA's less than this value. Such devices also provide time and direction resolution. Their sensitivity exceeds that of an ion chamber and geiger counter under comparable conditions since energy-loss measuring devices can observe the differential energy spectrum in the energy region of response. In this region, the solar cosmic rays can often be distinguished from the galactic by their rapid decrease in number with increasing energy. Also in this category are nuclear emulsions which provide energy, charge, and direction resolution and sensitivity equal to or surpassing that of the counters. Emulsions do not provide the time resolution, which is important in many aspects of solar-flare-particle study. Also, the need to recover emulsions limits their use to balloons and local rockets.

INDIRECT DETECTORS

Most indirect detectors respond to the ionization and resultant radiowave absorption produced by the solar cosmic rays in the 40- to 100-km level in the ionisphere. Although at this level the equilibrium electron density resulting from cosmic rays is smaller than in the E and F layers, the large collision frequency makes the product of collision frequency and density sufficient to produce appreciable absorption even at frequencies as high as 30 Mc/s. Some of the techniques used to measure the effects of this ionization are described below.

Measurement of Cosmic Noise Absorption

A self-balancing receiver called a riometer is used to measure the signal strength of extraterrestrial radio noise. The increased electron density caused by the solar cosmic rays absorbs the extraterrestrial noise more effectively and consequently decreases the signal measured at the ground.

In Fig. 5 (Ref. 4) the total absorption at 30 Mc/s is shown as a function of the spectrum and intensity of the solar particles (assuming protons only) for values of the effective cutoff rigidity appropriate to locations of various observing stations. Using the absorption measurements from a single station, we cannot determine either the spectrum or the intensity of the solar particles. If we have other intensity measurements, e.g., direct particle measurements, then we may determine both the spectrum and the intensity as precisely as we can calculate the absorption due to a spectrum of solar particles. The main uncertainty here lies in the ionospheric parameters and processes that determine the equilibrium electron density. Recent advances in our understanding of these parameters and processes have reduced the uncertainty in intensities calculated in this manner from a factor of about ten to a factor of two or less (Ref. 14).

The spectrum of solar particles can be determined by use of riometers located at several different latitudes as well as by use of

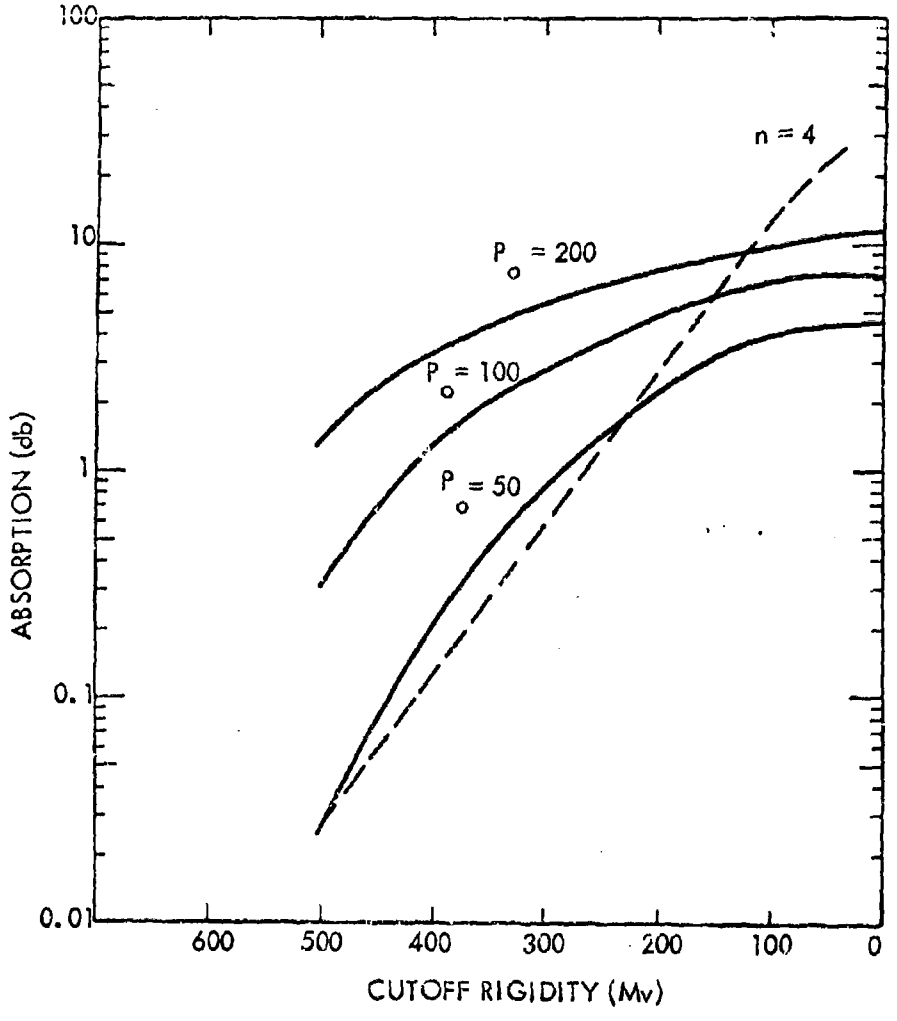

FIGURE 5. Absorption of radiowaves at 30 Mc/s as a function of rigidity for J_o = 1000 protons/cm^{2}ster-sec for various spectra of solar-cosmic-ray particles.

riometers operating at several different frequencies at a single location.

There is a difficulty in the interpretation of riometer data because ionization produced by particles not directly related to the solar cosmic rays also absorbs extraterrestrial radio noise. The absorption responsible for this problem is created mainly by auroral particles. This auroral absorption is generally less regular in both its temporal and spatial characteristics and hence is separable from solar-cosmic-ray absorption.

Measurement of f_{min}

In this technique, a radio station determines the minimum signal frequency which can be sent out from the earth, reflected at vertical incidence, and received back at the sending station. This signal is generally reflected from the E or F layer. Thus, a measurement of f_{min} is essentially a measure of the absorption taking place at the lower levels and is closely related to the results of absorption measurements by riometers. A large network of stations make f_{min} measurements. In some instances, the observations extend back to 1938. Hence, the record of these observations provides one of the best available monitors of the occurrence frequency of solar-cosmic-ray events. A quantitative basis of the f_{min} determinations is difficult to find since each station may have a somewhat different signal detection limit. Nevertheless, we show in Fig. 6 a typical

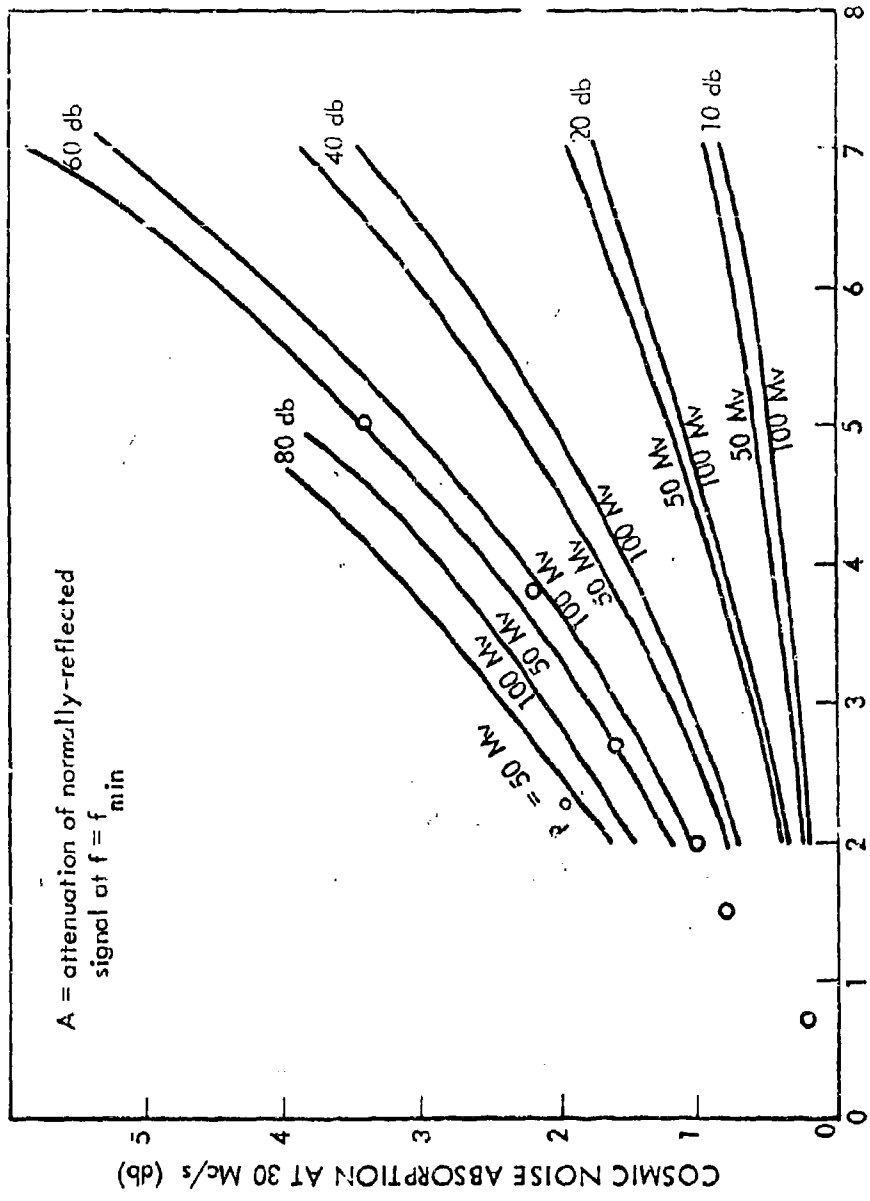

FIGURE 6. Cosmic noise absorption at 30 Mc/s as a function of Δf_{mir} for various particle rigidities and reflected-signal attenuations.

relation between the absorption of 30 Mc/s and the change in f_{min} from its normal value in the quiet ionosphere. Normal values of f_{min} are usually less than 1 Mc/s.

The attenuation of the f_{min} signal due to ionization below the reflecting layer is plotted as a parameter. Curves for exponential solar-particle rigidity spectra with average rigidities P_o = 50 and 100 Mv are shown. It is apparent that Δf_{min} is not a strong function of P_o. Experimental measurements of Δf_{min} and of the absorption at 30 Mc/s in one event are shown by the open circles in Fig. 6 (Ref. 15). These lie along a curve which suggests for the f_{min} receiver a detection capability of -60 db in this instance. Furthermore, this curve has an average slope of about 1 Mc/s change in f_{min} for each 0.6 db absorption at 30 Mc/s. Hence, this method of measuring is comparable in sensitivity to riometer measurements of cosmic noise absorption. Measurements of f_{min} could be improved, however, by increasing the sensitivity of the receivers or by actually measuring the strength of the returning signal.

By this method, just as by the riometer methods, ionization due to auroral particles can be mistaken for that produced by solar-cosmic-ray events.

Forward-Scatter Techniques

In this method, pioneered by Bailey (Ref. 16), a signal is reflected

at grazing incidence from the E or F layer. Reflection from a shallow angle of incidence is equivalent to scattering through a small angle, hence the term forward scattering. The attenuation of the remotely received signal is a measure of the absorption in the reflecting layer. This method is more sensitive to low levels of absorption because of the very long signal path through the absorbing layer. Also, it effectively discriminates against spatially localized auroral absorption. However, this method has not as yet been put on a quantitative basis.

In conclusion, in Table 1 we compare the capabilities of these various methods of detection for spectra with P_o = 50 and 100 Mv. For each method, we assume the smallest detectable response due to solar cosmic rays and translate this into a corresponding flux, J_o, of solar cosmic rays. The integral and differential measurements at 100 Mev correspond to typical balloon capabilities. The values listed for integrated intensity above 30 Mev refer to typical satellite measurements. Measurements of integrated intensity above 10 Mev and differential intensity at about 30 Mev represent the current best satellite achievements. These are somewhat better than the achievements of current radio techniques.

TABLE 1. Comparison of Detection Capabilities for Solar-Cosmic-Ray Particles

Method	Minimum Observable Change	Corresponding J_o	
		P_o = 50 Mv	P_o = 100 Mv
		(particles/cm^2-sec)	
Neutron Monitor	± 5 %	-	300,000
f_{min}	± 1 Mc/s	480	120
Riometer (30 Mc/s)	± 0.5 db	330	85
Balloon-borne detectors			
Measuring integrated intensity > 100 Mev	± 25 %	75,000	1,000
Measuring differential intensity at 100 Mev	± 50 %	3,000	100
Satellite-borne detectors			
Measuring integrated intensity > 30 Mev	± 25 %	1,500	140
Measuring integrated intensity > 10 Mev	± 25 %	180	40
Measuring differential intensity at 30 Mev	± 50 %	75	10

GENERAL DETAILS OF SOLAR-COSMIC-RAY EVENTS

The number of solar-cosmic-ray events observed depends closely on the techniques employed to observe them. In Table 2 we present a yearly record of observed events extending back to 1942. Prior to 1952, only f_{min} observations are available. Different observers using this technique agree quite closely on the number of events reported. From 1952 on, forward-scatter observations are available. From 1956, riometer observations have been made. Both of these methods have yielded a yearly frequency of events which is comparable to, but slightly less than, that found by f_{min} techniques. Although the sensitivities of all these methods are approximately the same, on the basis of f_{min} techniques alone, we may falsely identify as solar-cosmic-ray events a few instances of increased ionization due to other causes.

Satellite and space probe observations have been available since 1960. Consequently, the number of reported events has increased. The total number of events refers to all separate events identified by any technique. About 70 events have been observed at a given sensitivity of detection, comparable to the sensitivity of the f_{min} technique, in the solar cycle (cycle 19) just being completed. In the previous cycle, approximately 30 events were observed. On the basis of measurements since 1960, we estimate approximately 100 events would have been observed during

TABLE 2. Yearly Number of Solar-Cosmic-Ray Events as Observed by Different Techniques

Year	f_{min} (Ref. 17)	f_{min} (Ref. 15)	Riometer (Ref. 18)	Forward Scatter (Ref. 16)	Satellites (Ref. 19)	Total	
1942							
1943	0					0	
1944	0					0	
1945	0					0	
1946	6					6	
1947	4					4	
1948	4					4	
1949	7	7				7	
1950	3	5				5	
1951	1	3				3	
1952	0	0		0		0	
1953	0	1		1		1	
1954	0	0		0		0	
1955	1	1		0		1	
1956	5	6	2	3		6	
1957	14	14	13	11		16	
1958	12	15	10	10		15	
1959	7	8	5	5		10	
1960		14	11	14	20	14*	20**
1961		5	7		8	7*	8**
1962		1			3	1*	3**

Total for solar cycle 18 (February 1944 - April 1954) = 30 events

Total for solar cycle 19 (April 1954 -) = { 70 events / 100 events*** }

* Not including satellite data.
** Including satellite data.
*** Estimated from satellite data 1960-1962.

cycle 19 to date, had sensitivities been the same as in the satellite space-probe era. Although cycle 19 will not end until 1964, the total number of events reported here are expected to change very little, as we are now in the time of solar minimum when a solar event is a rare occurrence.

Of the events reported during cycle 19, the 52 largest are described in greater detail for the period 1956-1962 in Table 3. It is almost certain that all events with an integrated intensity greater than 10^6 particles/cm^2 above 30 Mev are included in the table and events to as low as approximately 2×10^5 particles/cm^2 above this energy are included. This is close to the lower size limit, which is presently determined by the integral satellite techniques. (This lower limit of intensity is about equal to the intensity of galactic cosmic rays integrated over one day.)

Most of the headings in the table are self-explanatory, but we can make the following remarks to elaborate.

The integrated RF emission of a solar flare listed in Table 3 is obtained from intensity-time profiles. An intensity-time profile is a plot of power density per unit bandwidth at a single frequency, usually 10,000 Mc/s. The peak emission listed in Table 3 is the maximum recorded on the same intensity-time profile. The frequency of peak emission in the microwave region is not necessarily the same frequency at which intensity as a function of time was recorded.

TABLE 3. Solar Flare Data (1956)

(Numbers in parentheses refer to footnotes appearing at end of table)

Date	February 23	March 11	August 31	November 13
Class	3+	n.d.(12)	3	2
Position(1)	22°N74°W	n.d.	16°N16°E	16°N10°W
$T_{opt\ max}$(2)	0340	n.d.	1241	1301
Max RF(3)	20000 at 0341			
$\int$(RF)(4)				
τ_{rise}(5)				
> 30 Mev	6			
> 100 Mev	3			
τ_{decay}(6)				
> 30 Mev	30	Uncertain	36(e)(13)	Uncertain
> 100 Mev	16			
Peak I(7)				
> 10 Mev	10000			
> 30 Mev	8000		150	
> 100 Mev	5000		60	
Peak P_o(8)	300		200	
$\int$(I)(9)				
> 10 Mev	1.8×10^9			
> 30 Mev	1.0×10^9		2.5×10^7	
> 100 Mev	3.5×10^8		6×10^6	
($\int$) P_o(10)	260		160	
p/a(11)				

TABLE 3. Solar Flare Data (1957)

Date	Jan 20	Apr 3	June 22	Jul 3	Aug 9
Class	3+	3		3+	
Position[1]	25°S30°W	15°S60°W	Uncert	14°N40°W	Uncert
$T_{opt\ max}$[2]	1120	0835		0740	
Max RF[3]				2400	
$\int(RF)$[4]					
τ_{rise}[5]					
> 30 Mev					
>100 Mev					
τ_{decay}[6]					
> 30 Mev	24(e)	Uncert	Uncert	30(e)	18(e)
>100 Mev					
Peak I[7]					
> 10 Mev					
> 30 Mev	2000(e)			200	20(e)
>100 Mev	100(e)				
Peak P_o[8]	70			50(e)	50(e)
$\int(I)$[9]					
> 10 Mev					
> 30 Mev	2×10^8			2×10^7	1.5×10^6
>100 Mev	7×10^6				
$(\int)P_o$[10]					
p/a[11]					

TABLE 3. Solar Flare Data (1957 Cont'd)

Date	Aug 29	Sep 21	Oct 20	Nov 4
Class		3	3+	
Position[1]	Uncert	10°N06°W	26°S45°W	n.d.
$T_{opt\ max}$[2]		1338	1642	
Max RF[3]		1100		
$\int(RF)$[4]				
τ_{rise}[5]				
> 30 Mev				
>100 Mev				
τ_{decay}[6]				
> 30 Mev	60(e)	24(e)	30(e)	18(e)
>100 Mev				
Peak I[7]				
> 10 Mev				
> 30 Mev	600	100(e)	500(e)	50(e)
>100 Mev	30		140(e)	
Peak P_o[8]	70(e)	50(e)	90(e)	50(e)
$\int(I)$[9]				
> 10 Mev				
> 30 Mev	1.2×10^8	1.5×10^6	5×10^7	9×10^6
>100 Mev	3×10^6		1×10^7	
$(\int)P_o$[10]				
p/a[11]				

TABLE 3. Solar Flare Data (1958)

Date	Feb 9	Mar 23	Apr 10	July 7
Class	2+	3+		3+
Position[1]	12°S14°W	14°S78°E	Uncert	25°N08°W
$T_{opt\ max}$[2]	2142	1005		0115
Max RF[3]		10000 at 1004		2000 at 0112
$\int(RF)$[4]				120
τ_{rise}[5]				
> 30 Mev				
>100 Mev				
τ_{decay}[6]				
> 30 Mev	18(e)	40		32
>100 Mev		20		16
Peak I[7]				
> 10 Mev		8000 (420)		1000
> 30 Mev	1000(e)	1200(60)	50	1500
>100 Mev		100 (1.2)		100
Peak P_o[8]	50(e)	75	50(e)	70
$\int(I)$[9]				
> 10 Mev		2×10^9 (3.5×10^7)		1.8×10^9
> 30 Mev		2.5×10^8 (7×10^6)	5×10^6	2.5×10^8
>100 Mev		1×10^7 (8×10^4)		9×10^6
$(\int)P_o$[10]		55		60
p/α[11]		1.5 ± 0.5		

TABLE 3. Solar Flare Data (1958 Cont'd)

Date	Aug 16	Aug 22	Aug 26	Sep 22
Class	3+	3	3	
Position[1]	14°S50°W	18°N10°W	20°N54°W	Uncert
$T_{opt\ max}$[2]	0440	1448	0027	
Max RF[3]	6200 at 0442		6700 at 0025	
$\int(RF)$[4]	600		700	
τ_{rise}[5]				
> 30 Mev	10	10		
>100 Mev		3		
τ_{decay}[6]				
> 30 Mev	18	20	12	30(e)
>100 Mev		8		
Peak I[7]				
> 10 Mev	3000	6000	15000	600
> 30 Mev	400	600	1500	50
>100 Mev	20	20	50	1.5
Peak P_o[8]	60	50	50	40
$\int(I)$[9]				
> 10 Mev	4×10^8	8×10^8	1.5×10^9	9×10^7
> 30 Mev	4×10^7	7×10^7	1.1×10^8	6×10^6
>100 Mev	1.6×10^6	1.8×10^6	2.0×10^6	1×10^5
$(\int)P_o$[10]				40
p/a[11]				

TABLE 3. Solar Flare Data (1959)

Date	May 10	June 13	July 10
Class	3+	1+	3+
Position[1]	23°N47°E	17°N57°E	22°N70°E
$T_{opt\ max}$[2]	2118	0400	0222
Max RF[3]	10000		20000 at 0224
$\int(RF)$[4]			1500
τ_{rise}[5]			
> 30 Mev	20		30
>100 Mev	10	24(e)	18
τ_{decay}[6]			
> 30 Mev	22		40
>100 Mev	14		20
Peak I[7]			
> 10 Mev	30000 (5000)		15000 (800)
> 30 Mev	6000 (500)	9(e)	4000 (160)
>100 Mev	1000 (5)		1200 (5)
Peak P_o[8]	70	50(e)	90
$\int(I)$[9]			
> 10 Mev	5.5×10^9 (7.5×10^8)		4.5×10^9 (1.6×10^8)
> 30 Mev	9.6×10^8 (4.2×10^7)	8.5×10^7	1.0×10^9 (2.4×10^7)
>100 Mev	8.5×10^7 (3.5×10^5)		1.4×10^8 (5×10^5)
$(\int)P_o$[10]	70		75
p/a[11]	1.5 ± 0.5		3 ± 1

TABLE 3. Solar Flare Data (1959 Cont'd)

Date	Jul 14	Jul 16	Aug 18
Class	3+	3+	3
Position[1]	16°N07°E	08°N26°W	12°N33°W
$T_{opt\ max}$[2]	0349	2145	1030
Max RF[3]	6300 at 0352	6500 at 2200	
$\int(RF)$[4]	800		
τ_{rise}[5]			
> 30 Mev	16	12	24(e)
>100 Mev	12	4	
τ_{decay}[6]			
> 30 Mev	18	30	
>100 Mev	12	18	
Peak			
> 10 Mev	50000 (10000)	18000 (5000)	20(e)
> 30 Mev	10000 (1000)	6000 (1500)	
>100 Mev	1200 (10)	1500 (100)	
Peak P_o[8]	70	110	
$\int(I)$[9]			
> 10 Mev	7.5×10^9 (1.3×10^9)	3.3×10^9 (7.5×10^8)	1.8×10^6(e)
> 30 Mev	1.3×10^9 (8×10^7)	9.1×10^8 (1.2×10^8)	
>100 Mev	1.0×10^8 (7×10^5)	1.3×10^8 (6×10^6)	
$(\int)P_o$[10]	60	100	
p/α[11]	1 ± 0.5	1 ± 0.5	

TABLE 3. Solar Flare Data (1960)

Date	Jan 11	Apr 1	Apr 5	Apr 28
Class	3	3	2+	3
Position[1]	23°N03°E	12°N10°W	10°N61°W	05°S34°E
$T_{opt\ max}$[2]	2100	0859	0245	0130
Max RF[3]			8000	
$\int(RF)$[4]				
τ_{rise}[5]				
> 30 Mev	6	1	3	3
>100 Mev		1		2
τ_{decay}[6]				
> 30 Mev	30	6	12	8
>100 Mev		4		5
Peak I[7]				
> 10 Mev		400		250
> 30 Mev	2.5	200	20	120
>100 Mev		45		25
Peak P_o[8]		150		240
$\int(I)$[9]				
> 10 Mev		1.5×10^7		1.3×10^7
> 30 Mev	4×10^5	5.0×10^6	1.1×10^6	5.0×10^6
>100 Mev		8.5×10^5		7×10^5
$(\int)P_o$[10]	100	130		150
p/a[11]				

TABLE 3. Solar Flare Data (U. 0 Cont'd)

Date	Apr 29	May 4	May	May 13
Class		3+	3	3+
Position[1]	Uncert	14°N90°W	10°S08°E	30°N64°W
$T_{opt\ max}$[2]		1020	1450	0536
Max RF[3]		200		8800
$\int(RF)$[4]		10		1200
τ_{rise}[5]				
> 30 Mev		2-3	3	3
>100 Mev		1		
τ_{decay}[6]				
> 30 Mev		14	24	15
>100 Mev		6		
Peak I[7]				
> 10 Mev		150		180
> 30 Mev	100	100	40	60
>100 Mev		40		10
Peak P_o[8]	60	300		90
$\int(I)$[9]				
> 10 Mev		1.2×10^7		1.5×10^7
> 30 Mev	7×10^6	6×10^6	4×10^6	4×10^6
>100 Mev		1.2×10^6		4.5×10^5
$(\int)P_o$[10]		200		85
p/a[11]				

TABLE 3. Solar Flare Data (1960 Cont'd)

Date	Jun 1	Aug 12	Sep 3	Sep 26
Class	3+	3+	3	2
Position[1]	28°N46°E	22°N27°E	18°N88°E	21°S64°W
$T_{opt\ max}$[2]	0844	1940	0110	0550
Max RF[3]			12000 at 0108	
$\int(RF)$[4]			400	
τ_{rise}[5]				
> 30 Mev	2	10	12	n.d.
>100 Mev			6	
τ_{decay}[6]				
> 30 Mev	20	50	32	
>100 Mev			26	
Peak I[7]				
> 10 Mev			450 (6)	300
> 30 Mev	5	3	200 (3)	40
>100 Mev			60 (0.4)	4
Peak P_o[8]			180	65
$\int(I)$[9]				
> 10 Mev			9×10^7 (1×10^6)	2×10^7
> 30 Mev	4×10^5	6×10^5	3.5×10^7 (3.6×10^5)	2×10^6
>100 Mev			7×10^6 (4×10^4)	1.2×10^5
$(\int)P_o$[10]			160	60
p/α[11]			20 ± 7	

TABLE 3. Solar Flare Data (1960 Cont'd)

Date	Nov 12	Nov 15	Nov 20
Class	3+	3+	3
Position[1]	27°N02°W	30°N32°W	28°N113°W
$T_{opt\ max}$[2]	1329	0221	2020
Max RF[3]	10000 at 1329	14000 at 0227	1000
$\int(RF)$[4]	3400	2000	100
τ_{rise}[5]			
> 30 Mev	10	8	2
>100 Mev	8	4	1
τ_{decay}[6]			
> 30 Mev	18	16	10
>100 Mev	14	10	5
Peak I[7]			
> 10 Mev	32000 (4000)	22000 (4200)	2200
> 30 Mev	12000 (1500)	8000 (1500)	1000
>100 Mev	2500 (180)	2400 (160)	400
Peak P_o[8]	145	135	180
$\int(I)$[9]			
> 10 Mev	4×10^9 (4×10^8)	2.5×10^9 (3.8×10^8)	1.4×10^8
> 30 Mev	1.3×10^9 (1.2×10^8)	7.2×10^8 (9×10^7)	4.5×10^7
>100 Mev	2.5×10^8 (1.1×10^7)	1.2×10^8 (6.5×10^6)	8×10^6
$(\int)P_o$[10]	135	125	140
p/a[11]	2 ± 0.5	1.8 ± 0.5	

TABLE 3. Solar Flare Data (1961)

Date	Jul 11	Jul 12	Jul 18
Class	3	3+	3+
Position[1]	06°S32°E	07°S22°E	06°S60°W
$T_{opt\ max}$[2]	1700	1030	1015
Max RF[3]	2500	7500	5000
$\int(RF)$[4]		850	300
τ_{rise}[5]			
> 30 Mev	8-10	8-12	6-10
>100 Mev	4	24	2-3
τ_{decay}[6]			
> 30 Mev	22-26	16-20	24
>100 Mev	18	12	12
Peak I[7]			
> 10 Mev	120	4000	7000 (280)
> 30 Mev	30	400	2500 (100)
>100 Mev	3	15	60 (11)
Peak P_o[8]	70	50	135
$\int(I)$[9]			
> 10 Mev	1.7×10^7	5×10^8	1×10^9 (3×10^7)
> 30 Mev	3×10^6	4×10^7	3×10^8 (5.5×10^6)
>100 Mev	2.4×10^5	1×10^6	4×10^7 (4×10^5)
$(\int)P_o$[10]	60	40	110
p/a[11]			6 ± 1

TABLE 3. Solar Flare Data (1961 Cont'd)

Date	Jul 20	Sep 28	Nov 10
Class	3+	3	2+
Position[1]	07°S90°W	14°N30°E	08°N90°W
$T_{opt\ max}$[2]	1600	2223	1444
Max RF[3]	2500	700	
$\int(RF)$[4]		24	
τ_{rise}[5]			
> 30 Mev	4-6	1.5	
>100 Mev	1.5	1	
τ_{decay}[6]			
> 30 Mev	6-8	12	
>100 Mev	4	8	
Peak I[7]			
> 10 Mev	400	500	
> 30 Mev	150	150	
>100 Mev	40	36	
Peak P_o[8]	150	210	
$\int(i)$[9]			
> 10 Mev	1.5×10^7	5×10^7	
> 30 Mev	5×10^6	6×10^6	
>100 Mev	9×10^5	1.1×10^6	
$(\int)P_o$[10]	130	140	
p/a[11]			

TABLE 3. Solar Flare Data (1962)

Date	Feb 4	Oct 23
Class	3	2
Position[1]	10°N80°W (Uncert)	02°N71°W
$T_{opt\ max}$[2]	0222	1708
Max RF[3]		160
$\int(RF)$[4]		
τ_{rise}[5]		
> 30 Mev		2
>100 Mev		
τ_{decay}[6]		
> 30 Mev		8
>100 Mev	Uncert	
Peak I[7]		
> 10 Mev		16
> 30 Mev		4.5
>100 Mev		0.5
Peak P_o[8]		80
$\int(I)$[9]		
> 10 Mev		6×10^5
> 30 Mev		1.2×10^5
>100 Mev		1×10^4
$(\int)P_o$[10]		70
p/a[11]		

TABLE 3. Solar Flare Data (Cont'd)

Footnotes

(1) Heliographic position in degrees.

(2) Time of optical maximum in UT.

(3) Maximum radio emission at a frequency in the range from 3000 to 10000 Mc/s. The emission is given in units of 10^{-22} watts/m^2-cps at a time, if known, in UT.

(4) Time-integrated radio emission at a frequency in the range from 3000 to 10000 Mc/s in units of 10^{-18} joules/m^2-cps.

(5) Onset plus rise time in hours for two energy groups.

(6) Decay time in hours for two energy groups.

(7) Peak omnidirectional proton intensity in units of particles/cm^2-sec above various energies. Values in parentheses are alpha particle intensities in units of particles/cm^2-sec above various energies per nucleon.

(8) Characteristic peak P_o in Mv measured at time of peak intensity of 10-Mev particles.

(9) Time-integrated omnidirectional proton intensity in units of particles/cm^2 above various energies. Values in parentheses are alpha particle intensities in units of particles/cm^2 above various energies per nucleon.

(10) Characteristic integrated P_o in Mv estimated from all available measurements, direct and indirect.

(11) Proton/alpha ratio given for some rigidity.

(12) No data.

(13) (e) Indicates estimated value.

The integrated intensity above a given energy is calculated using the characteristic rise and decay times according to

$$J(>E) = \int_{-\infty}^{0} I_{max}(>E)\, \exp(-t/t_R)\, dt + \int_{0}^{\infty} I_{max}(>E) \exp(-t/t_D)\, dt$$

$$= (t_R + t_D)\, I_{max}(>E)$$

Here $t = 0$ is the time of maximum intensity of the appropriate energy particles. The values of I_{max} are also listed in the table. The intensity-time characteristics for protons and alpha particles are assumed to be the same. When an event does not show such a characteristically simple intensity-time behavior, a step-by-step integration of the intensity-time profile has been made to obtain the integrated intensity (e.g., November 12, 1960).

The integrated intensities also appear to exhibit exponential rigidity spectra. The characteristic P_o of this spectrum is close to, but slightly smaller than, that of the spectrum at peak intensity and is called the characteristic integrated P_o.

When measurements are available from two or more techniques, it may be possible to estimate roughly such quantities as decay and rise times, peak intensities, and characteristic rigidities. These estimates are followed by an (e) in Table 3 and have a greater uncertainty than values of these quantities in events for which more data are available. In some cases, it

is possible to ascertain only that an event has occurred. No estimates of size can be made except to say that these events are generally smaller ones. We simply report these as uncertain.

A number of features of the solar-cosmic-ray events can be deduced from Table 3. Some of the most interesting properties will be described.

ENORMOUS VARIATIONS

An enormous variation in integrated-particle intensity is observed. For particles above 30 Mev, the integrated intensity may range from about 10^5 particles/cm^2 to about 10^9 particles/cm^2. The number of events of a given size, i.e., the differential size spectrum, does not appear to increase rapidly with decreasing size but seems to peak at about 10^7 particles/cm^2 and flatten off or even decrease for sizes smaller than this. This result may be due in part to a lack of sensitivity in detecting the smaller events and in determining their size. However, it may be a real effect since we believe our probability of not detecting events with an integrated intensity greater than 10^6 particles/cm^2 at energies above 30 Mev is negligible small. Furthermore, an increase in sensitivity, which allows detection of events with about 10^5 particles/cm^2 by use of satellite measurements, causes about a 30 percent increase in the number of events observed. We base the 30 percent figure on 1960-1962 data. This

proportion of events, added to the differential spectrum shown in Fig. 7, makes the distribution flat, but is not suggestive of any rapid increase in number versus size at smaller sizes. This size distribution, shown also in integral form in Fig. 8, has important implications for a statistical calculation of the integrated intensities of particles received over relatively long periods. In effect, such a distribution implies that the probability of receiving a dangerous dose depends on the probability of encounter with a large event and that the addition of small events is not a serious problem.

ASSOCIATION WITH ACTIVE CENTERS

We note that, although 52 separate events are catalogued, they occurred in only 34 active centers. During the three years from 1959 through 1961, this effect was even more pronounced: 27 separate events are associated with 15 active centers. Usually, the active centers associated with the cosmic-ray-producing flares were already well developed when they appeared on the east limb of the sun. Only once after a major event has the same active center continued to produce cosmic-ray events on its subsequent appearance on the visible portion of the sun. We are thus motivated to group the cosmic-ray events according to active centers. During solar cycle 19, eight centers have each produced, within a period of a week, in excess of 10^9 particles/cm^2

THIS

PAGE

IS

MISSING

IN

ORIGINAL

DOCUMENT

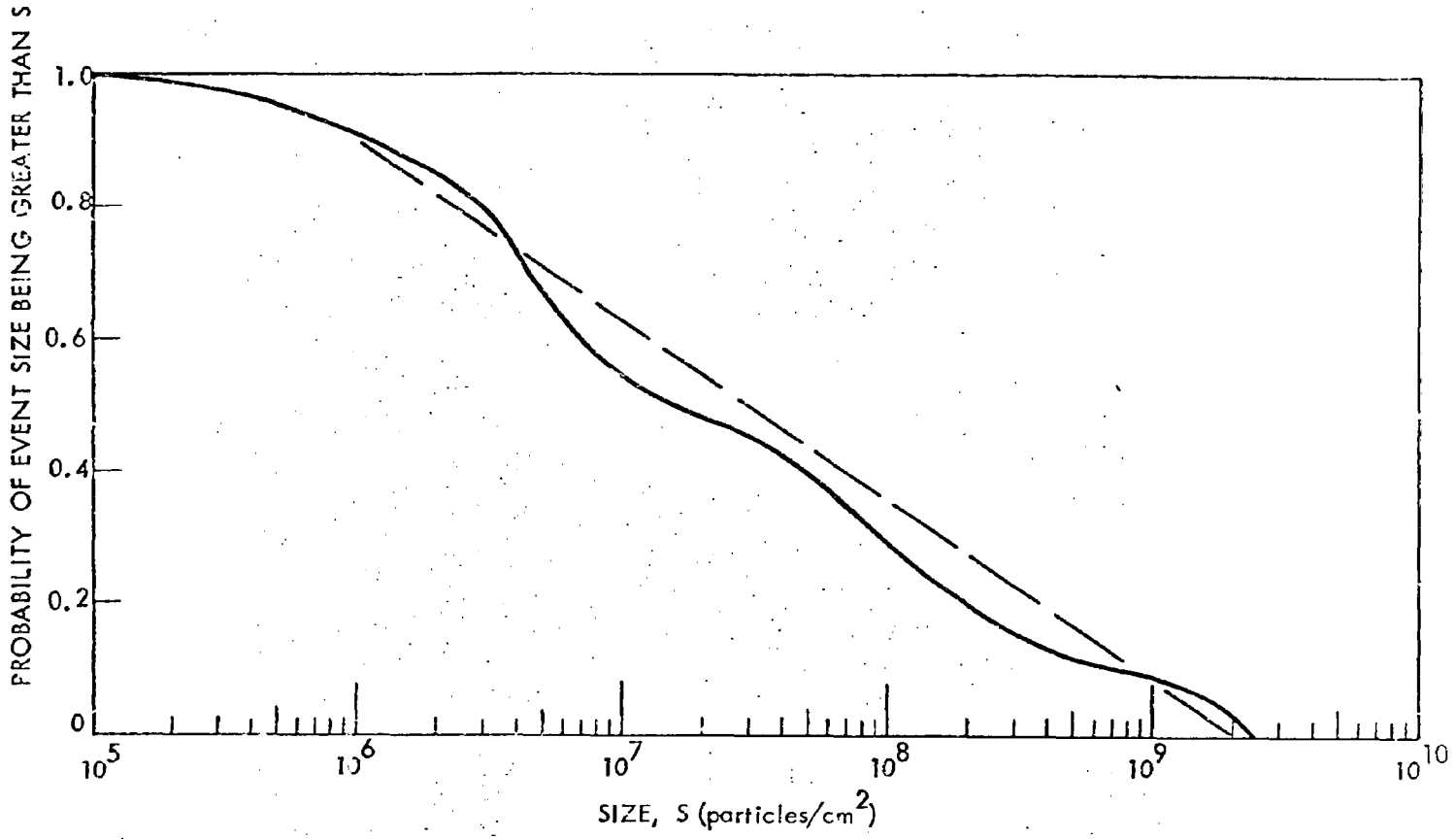

FIGURE 8. Integral size distribution for particles of energies greater than 30 Mev for all events listed in Table 3.

above 10 Mev at the earth. The intensities produced by these centers exceed the yearly intensities of galactic cosmic rays by a factor of ten. The output of cosmic rays above 10 Mev from these eight active centers is about 90 percent of all the solar cosmic rays above this energy produced during this cycle. These eight major events are listed year by year in Table 4. Although none of these major events occurred in 1957 at the peak of the sunspot cycle, the correlation of the frequency of these events with sunspot number is much better than the similar correlation of the frequency of events observed at sea level. Sea-level events appear to occur more frequently on the increasing and decreasing parts of the cycle (Ref. 2).

EAST-WEST ASYMMETRY

Of events for which we are able to make a size estimate and also to know the location of the producing flare on the sun, 29 have come from flares on the sun's western hemisphere and 8 from the eastern. Of these same events, 24 have come from flares in the northern hemisphere and 12 from the southern. The north-south asymmetry depends partly on a few active centers and may not be real. The east-west asymmetry, which has been pointed out previously (Refs. 3 and 6), is of great significance, however. This effect, which is undoubtedly a propagation effect through interplanetary space, holds for all size groups, not just the largest events.

TABLE 4. The Eight Largest Solar-Cosmic-Ray Outbursts During Cycle 19

Year	Number of Events	Dates
1954	0	
1955	0	
1956	1	February 23
1957	0	
1958	3	March 26, July 7, August 16-26
1959	2	May 10, July 10-16
1960	1	November 12-15
1961	1	July 12-18
1962	0	
1963	0	

This peculiar result, which may follow from the rather flat size distribution of events, means that flares occurring in active regions on the eastern hemisphere of the sun are about one-third as likely to produce a cosmic ray event (of any size) observed at the earth. In addition, the average onset-delay and rise times for cosmic rays from flares on the east hemisphere of the sun are about three times as long as from the western hemisphere.

This situation suggests that, on the average, a greater fraction of the emitted particles is received at the earth when the flare is on the western hemisphere of the sun.

ALPHA PARTICLES AND HEAVIER NUCLEI

In many events, alpha particles and heavier nuclei, principally C, N, O, and Ne, have been observed in considerable numbers (Refs. 7 and 8). These particles appear to have the same rigidity spectrum as the protons and have essentially the same intensity-time characteristics as the protons if the comparison is on a rigidity basis. These facts suggest that the interplanetary control mechanism sorts the particles according to rigidity. The ratio of protons to alphas above a fixed rigidity varies widely, whereas the alpha to heavier nuceli ratio, based on only three events, appears to be a constant, approximately sixty. Most commonly, the value for the proton-alpha ratio lies between one and two, although events with a ratio around 20 have been observed. Even at a ratio of

difficult to detect since, at a fixed rigidity, their [illegible] is substantially less than that of protons. This detection problem particularly hampers balloon observations, and, for this reason, the alphas have been observed only during the largest events. It is quite possible that the proton-alpha ratio increases with decreasing event size. Then the preponderance of ratios in the range from one to two would be misleading. In fact, there is some evidence for this increase. In at least two of the smaller events (July 12, 1961 and September 28, 1961), an absence of observed alphas implies, within the limits of detection, proton-alpha ratios greater than five. Integrated fluxes of alphas with energy greater than 30 Mev/nucleon were observed to be about $2.5 \times 10^8/cm^2$ during the July 1959 events. During the November 1960 events, this intensity reached $2.2 \times 10^8/cm^2$. These values amount to about 10 percent of the flux of protons with the same energy range in these events and to about three times the total galactic-particle flux integrated over one year. In the November 1960 event, we assume that the particles heavier than alphas had the same intensity-time profile as the alphas. Then the total integrated intensity of such nuclei with energies greater than 30 Mev/nucleon was about $3 \times 10^6/cm^2$.

SUMMARY OF OBSERVED INTENSITIES OF SOLAR COSMIC RAYS

By way of a general summary of the intensities of solar cosmic rays, we show in Table 5 the yearly integrated intensities of solar protons above 10, 30, and 100 Mev, respectively. A similar table could be made for alphas, but since our information relates to only a few events, we have not attempted to make this compilation. It is seen from the table that the peak intensity of protons was observed in 1959 for all energy intervals. This maximum is due principally to the July events and again points up the importance of the single large event. The intensity, integrated over the entire solar cycle 19, is very nearly equal to the sum over the six years shown in the table and amounts to 9×10^9 particles/cm^2 above 30 Mev in free space. We estimate that, over the entire cycle, 2×10^{11} particles/cm^2 above 3 Mev would be observed near the earth. Also shown in this table are the P_o's characteristic of the spectra, based on the yearly integrated intensities. Notice that the P_o's are smaller (50 to 70 Mv) during the years near sunspot maximum. Accordingly, no sea-level events are observed during these years. However, the total yearly flux of all solar cosmic rays is highest during these years. The flatter spectra observed during the ascending and descending portions of the solar cycle are in keeping with observation of the greatest frequency of sea-level events during these periods, although the total yearly intensity is then somewhat

TABLE 5. Observed Yearly Integrated Intensities of Solar Protons

Year	Number of Events	Integrated Intensity			P_o
		E > 10 Mev	E > 30 Mev	E > 100 Mev	
		(protons/cm^2)			(Mv)
1956	4	2.0×10^9	1.0×10^9	3.5×10^8	250
1957	9	---	4.0×10^8	2.0×10^7	60
1958	8	7.0×10^9	7.8×10^8	2.4×10^7	50
1959	6	2.2×10^{10}	4.2×10^9	4.6×10^8	70
1960	15	6.8×10^9	2.2×10^9	3.8×10^8	130
1961	6	1.6×10^9	3.5×10^8	4.2×10^7	90
1962	2				
1963	1				
	52				
	Solar-cycle total	3.9×10^{10}	9.0×10^9	1.3×10^9	100 (av.)

less than in the peak period.

For environments near the surface of the earth, these data are presented in another way in Fig. 9. Here, the intensity is plotted as a function of geomagnetic latitude and the parameter L, which are related by $\cos^2 \lambda = 1/L$.

In Fig. 9 the curve labelled (a) is the integrated intensity of particles of all energies during the "worst" year in the recent sunspot cycle (flux in 1956 at high energies; 1959 at low energies); (b) is the average yearly intensity observed during the recent sunspot cycle; (1) is the envelope of the greatest single events, consisting of the July 1959 events at low energies (< 50 Mev), the November 1960 events at intermediate energies (50 to 150 Mev), and the February 1956 event at higher energies (> 150 Mev); (2) is the envelope of the second-largest single events, consisting of the November 1960 events at low energies, the July 1959 events at intermediate energies, and the November 1960 events again at higher energies; and (3) is the envelope of the third-largest single events, consisting of the May 1959 event at low energies, February 1956 at intermediate energies, and the July 1959 events at higher energies.

These plots show clearly the importance of the single large events as well as the effects of the particle spectra in the different events.

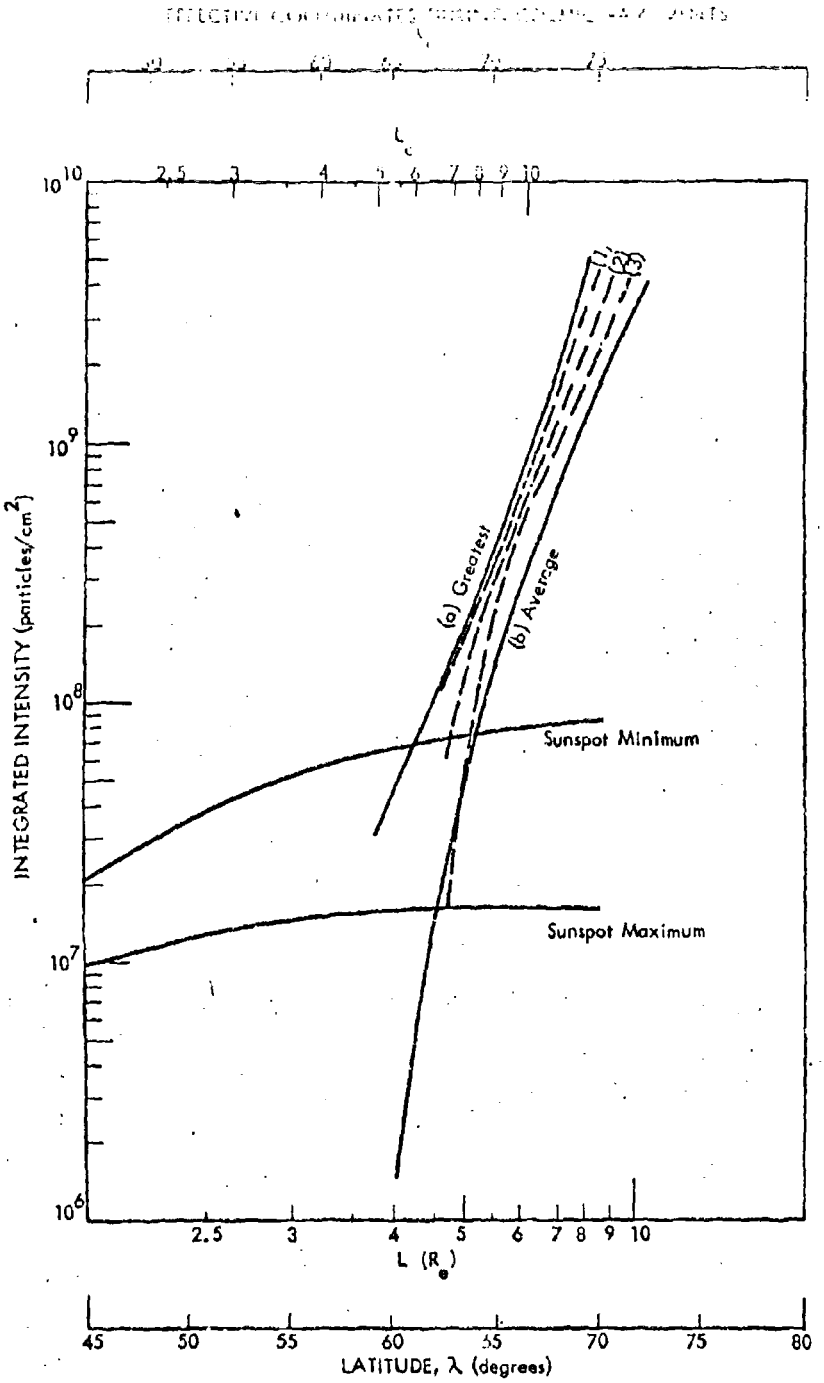

FIGURE 9. Intensity of solar cosmic rays as a function of latitude λ and and the L parameter. (See text for a discussion of the curves.)

Finally, we show in Fig. 9 the yearly integrated intensities of all galactic cosmic rays to be expected at both sunspot minimum and sunspot maximum. We see that above a nominal geomagnetic latitude of 65° or outside a magnetic shell with L = 5.5 (i.e., in the equatorial plane 5.5 times the radius of the earth), the intensities of solar cosmic rays dominate those of galactic particles in yearly averages. This domination holds true in all but the quietest years near sunspot minimum.

An important point should now be mentioned in connection with the spatial distribution of solar cosmic rays in the earth's magnetosphere. Experimental flux measurements are shown as a function of the conventional geomagnetic latitude on the lower scale of Fig. 9. From these measurements and with certain assumptions of isotropy, an energy or rigidity spectrum of the cosmic rays could be constructed if the geomagnetic field were at all times a simple dipole derivable entirely from sources within the earth. For example, if the geomagnetic field is assumed to be a dipole with a moment of 8.1×10^{25} gauss-cm^3, the cutoff (minimum) rigidity, P_c, for particles reaching the earth's surface at a given latitude λ is given by

$$P_c = 14.9 \cos^4 \lambda \text{ Gv.}$$

Such calculations agree reasonably well, at times when the sun is quiet (i.e., no solar cosmic rays), with direct spectral measurements. However, during solar events, ring currents in the magnetosphere and magnetic storms

due to currents just outside the magnetosphere decrease the cutoff rigidity at a given point. Calculations of the spectrum using geomagnetic coordinates would then be incorrect. On the average, during the arrival of solar cosmic rays at the earth, the cutoff rigidities at latitudes greater than 60° may be only about one-half of what is normally to be expected. Thus, detecting stations receive particles which, on the basis of dipole field calculations, would be expected only at latitudes about 5° higher than the actual geomagnetic latitude of the station. Equivalently, the solar particles reach lower latitudes and smaller L values than normally expected. This effect is variable from event to event, but an average correction is deemed suitable for the preceding kind of analysis and is shown as a set of effective latitudes and L values at the top of Fig. 9. The net effect is to move the latitude at which the solar cosmic rays dominate the galactic particles to about 60° as measured in the actual geomagnetic coordinates instead of 65° as predicted theoretically, and to change L from approximately 5.5 to 4. As a consequence, the magnetically-shielded region around the earth is shrunk.

PREDICTION CAPABILITIES FOR SOLAR-COSMIC-RAY EVENTS

The ability to predict the occurrence of a solar-cosmic-ray event is of prime importance in planning space missions. Prediction capabilities may be resolved into three rather distinct categories.

FEW-HOUR WARNING

Solar cosmic rays generally do not reach peak intensity until a number of hours after the source flare. If we can estimate reasonably from the size of a flare or from its accompanying electromagnetic emissions the integrated cosmic-ray intensity to arrive at the earth, then we could provide a warning several hours in advance of the solar-cosmic-ray event. During this time, astronauts could make special preparations and perhaps move an orbiting vehicle to less dangerous regions of space.

If we attempt to use flare size as a criterion, then we have the following data from solar cycle 19. During this cycle, a total of about 120 flares of class 3 or larger was observed. Of these, 33 were accompanied by solar-cosmic-ray outbursts. In this same period, of the approximately 1,100 class 2 flares which occurred, 6 were accompanied by cosmic-ray outbursts. Obviously, there is some correlation with flare size, but it is not a very strong criterion. We need an indicator that will give not only a high probability of predicting the occurrence of a cosmic-ray event, but

also some measure of the size of the cosmic-ray event. We believe that such a measure is provided by the correlation between the microwave (cm wave) output from the flare and the cosmic-ray intensity observed at the earth. In particular, we shall use for our correlation study the emission at 10,000 Mc/s. In Fig. 10, we show a regression curve of the peak emission at 10,000 Mc/s and the peak intensity of cosmic rays above 10 Mev at the earth. We see a strong correlation between these quantities; however, some events lie unusually far off the curve. A number of features could cause this scatter. First of all, this approach does not consider the obvious spectral differences of the events. Hence, comparison of radio emission at a fixed frequency and intensity of particles above a given energy may give different relations for different spectra. A regression curve similar to that in Fig. 10, but using the peak intensity of cosmic rays above 30 Mev, shows a wider scatter.

In addition, the intensity of cosmic rays near the earth depends strongly on the propagation conditions in interplanetary space and on the location of the flare on the sun. An east-limb flare might be expected to produce less cosmic-ray intensity at the earth than a west-limb flare of equal magnitude, for example.

In view of these difficulties, which are inherent in any warning process based in this general way on electromagnetic emission, we have

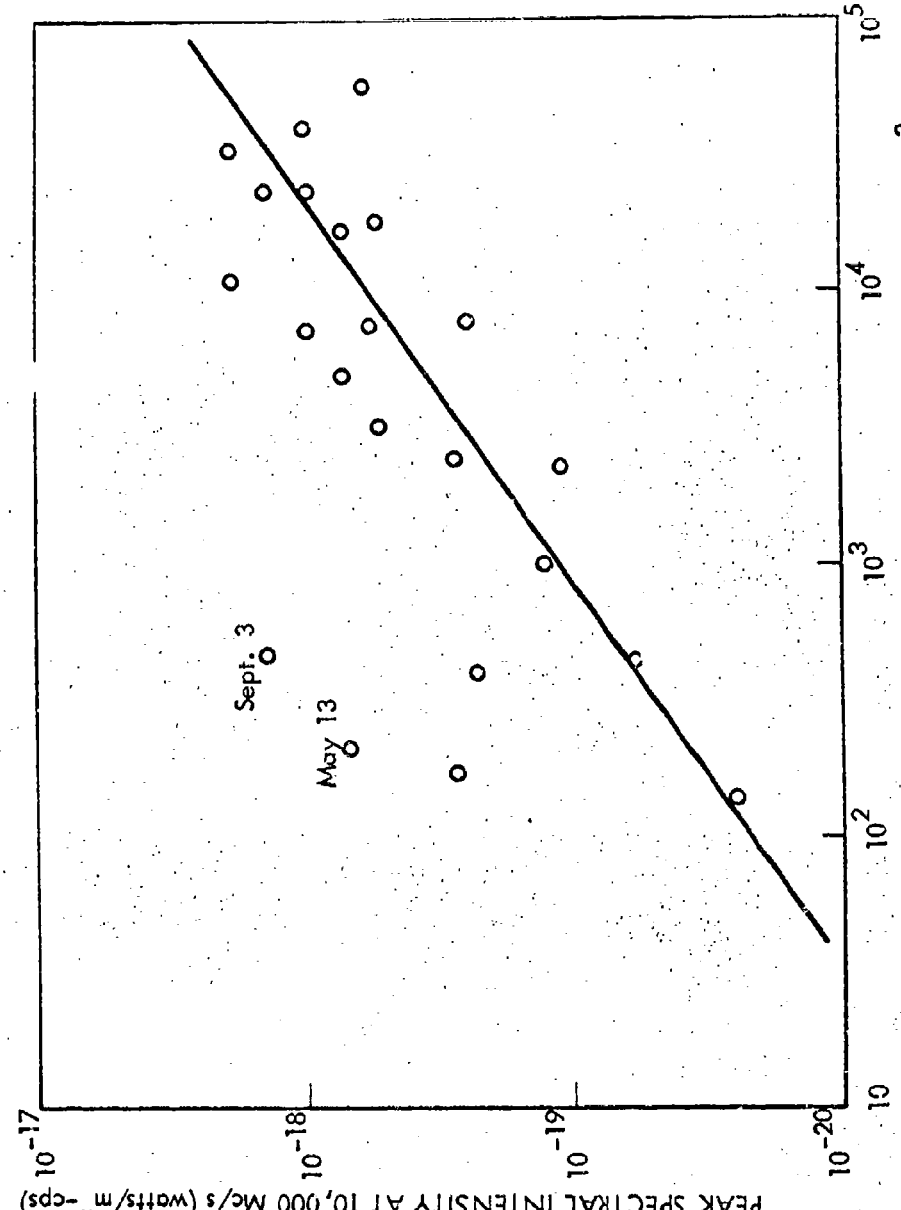

FIGURE 10. Peak radio emission at 10,000 Mc/s versus peak intensity of solar particles above 10 Mev at the earth for various events.

compared in Fig. 11 the integrated emission at 10,000 Mc/s with the integrated intensity of cosmic rays above 10 Mev observed at the earth. The correlation here is perhaps somewhat better than for the peak intensities, and, of course, the integrated intensity is a more useful quantity for the dose calculations. In fact, if we omit the two events which give one to two orders of magnitude less cosmic-ray intensity than the prediction indicated by their radio emission, we find that we can predict within a factor of three the integrated cosmic-ray intensity, given the integrated radio emission.

PREDICTIONS OF A FEW WEEKS OR LESS

The capability to predict a few weeks or less in advance would be valuable for orbital or lunar missions of this duration. We would use visible conditions on the sun and the possible occurrence of a cosmic-ray-producing event as basic factors. As we have seen, the presence and development of an active region with its associated sunspots and complex magnetic field is a basic part of the process which leads to a solar-cosmic-ray event. We have also seen that the larger events constitute the greatest hazard for any mission, at least for one of extended duration. Let us first examine the histories of twelve active centers which went on to produce the largest cosmic-ray events. Of these twelve centers, three produced major cosmic-ray events on their first passage across the visible

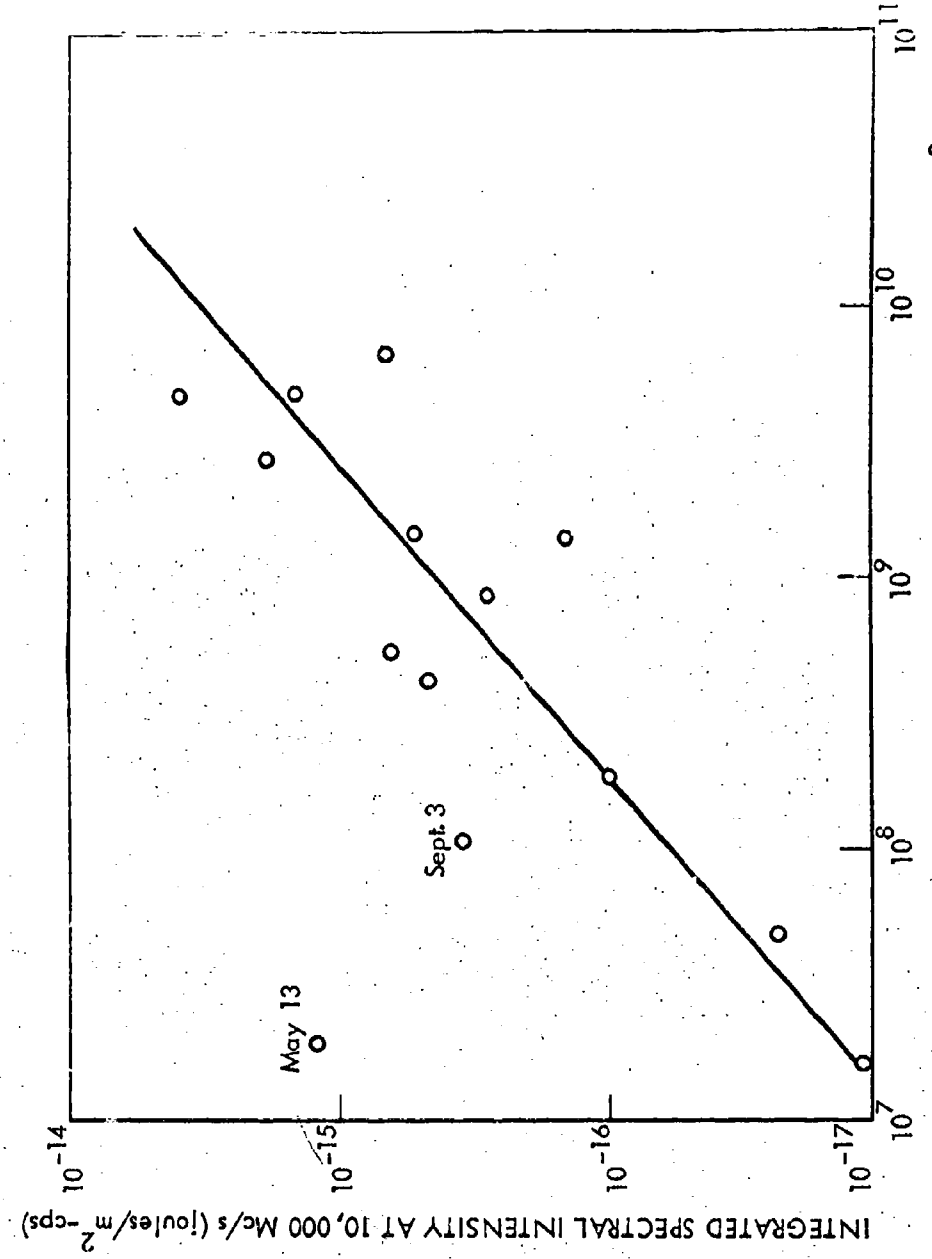

FIGURE 11. Integrated radio emission at 10,000 Mc/s versus integrated intensity of solar particles above 10 Mev at the earth for various events.

solar hemisphere, seven on their second passage, and one each on the third and fifth recorded passages. The average time from the birth of an active center to the production of solar cosmic rays thus seems to be a little less than two solar rotations (54 days).

Those events occurring on the first passage can give, at most, a few days' warning. In all these instances, the active center was fairly large and growing in size and intensity as it appeared at the east limb. In five cases where events occurred on the second passage, the associated active centers were sufficiently large and growing to seem as potentially dangerous as the centers which produced events on their first passage. The other two centers which produced second-passage events, including the November 1960 major-event group, were relatively inconspicuous. Of the two events occurring on the third and fifth passages of the associated active centers, the one in July 1959 was associated with a large and growing center but the other, May 1959, was associated with a weak center which persisted for four rotations and gave no special indications before it burst into cosmic-ray activity on its fifth rotation.

In addition, only two active centers have produced cosmic rays on more than one rotation.

All of the eight largest events in cycle 19 occurred on the second or a later passage of the associated active center. This gives us at least

a possibility of recognizing the potentially dangerous events perhaps a month ahead of time. Unfortunately, no reliable method has been devised for telling which of these active regions is potentially dangerous. We must resort to the simplest possible criterion, a criterion based on the size of the active center or of the sunspots making up the active center. If we adopt such an approach and set our criterion too low, then it is possible that no safe periods at all will be found near sunspot maximum. Application of this approach to selected years by Anderson (Ref. 20) shows that adopting a critical area of 1000×10^{-6} of that of the sun reduces the usable time to ~ 25 percent near sunspot maximum. This criterion also reduces the number of events encountered, but, unfortunately, not by a great deal more than the factor of four reduction in time. A study of selection criteria of this sort for various area limits reveals that if we are willing to accept a usable time between 25 and 50 percent of that available, then we can achieve over the sunspot cycle a factor of two to three decrease in frequency of solar-cosmic-ray events by means of the size criterion.

Another method of decreasing the frequency of encounter with a solar-cosmic-ray event makes use of the east-west asymmetry in the location of the flare on the sun and the cosmic-ray events observed at the earth. Figure 12 shows the number of cosmic-ray events observed at

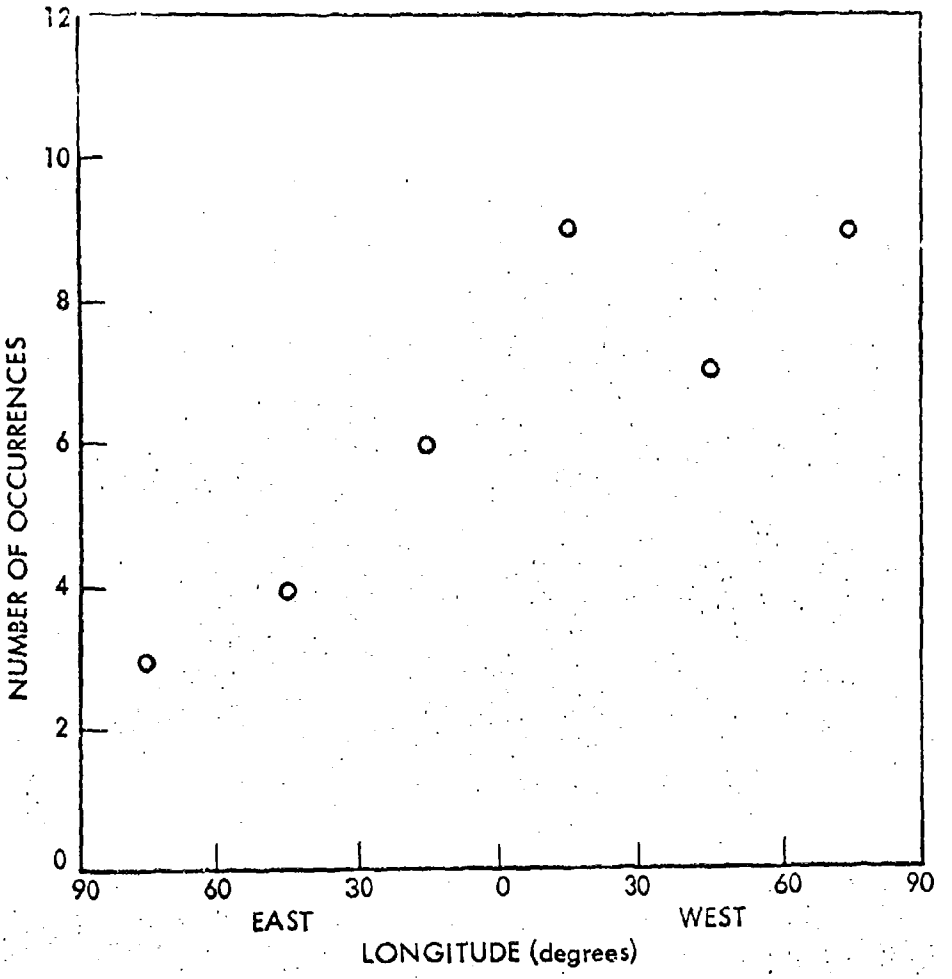

FIGURE 12. Occurrence of solar-cosmic-ray events c the earth as a function of longitude of the flare on the visible solar hemisphere.

the earth versus the longitude on the sun of the producing flare for cycle 19. We see that the probability of seeing cosmic rays from flares or active centers on the west quadrant is about three times greater than that from flares on the east quadrant. Missions may thus be conducted during the period where an active center is on the east quadrant with a decreased probability of encounter with a cosmic-ray event.

In summary, we may say that without a great deal of understanding of the processes causing cosmic-ray flares, we may still decrease our probability of encounter by a factor of five for intervals of one- to two-weeks' duration at the expense of reducing the available time by 50 percent. The necessary predictions can be made perhaps 30 days in advance by using relctively simple criteria such as development time, location, and size of flare-producing active centers.

Other systematic studies of the active centers may improve this prediction capability somewhat, but our understanding of the basic solar physics must be improved to provide a rigorous basis.

PREDICTIONS FROM MONTHS TO YEARS

A capability to predict for time intervals in excess of a few months and extending up to a number of years is needed to plan missions with lunar bases and for planetary missions which may take more than a year. This capability is necessarily based on an extrapolation of our knowledge of

the variation in the rate of occurrence of solar-cosmic-ray events during the sunspot cycle.

Let us first examine some relations between the solar-cosmic-ray events and certain features relating to the sunspot cycle. There are a number of solar features we could examine. These include (1) the sunspot number, (2) the yearly distribution of 3+ flares, and (3) the yearly distribution of microwave bursts above a certain intensity. Even though the sunspot number is not a good indicator of individual events, we suggest that sunspot number may be a useful indicator of the yearly integrated intensity of solar cosmic rays above, say, 10 Mev. The satisfactory correlation between these quantities is shown in Fig. 13 for the years from 1955 through 1962. This indicates that we can make estimates of the expected yearly intensities of cosmic rays from projections of yearly sunspot numbers. To investigate this correlation further and to extend the measurements over more than one solar cycle, we show in Fig. 14 a plot of the yearly number of solar-cosmic-ray events as a function of the yearly sunspot numbers for the years from 1942 through 1962. The number of cosmic-ray events is based on f_{min} data adjusted to a constant sensitivity of detection over the entire period. As we have pointed out, this adjustment should amount to at least a 30 percent increase to make the data comparable with that provided in the era of improved detection capabilities provided by satellites

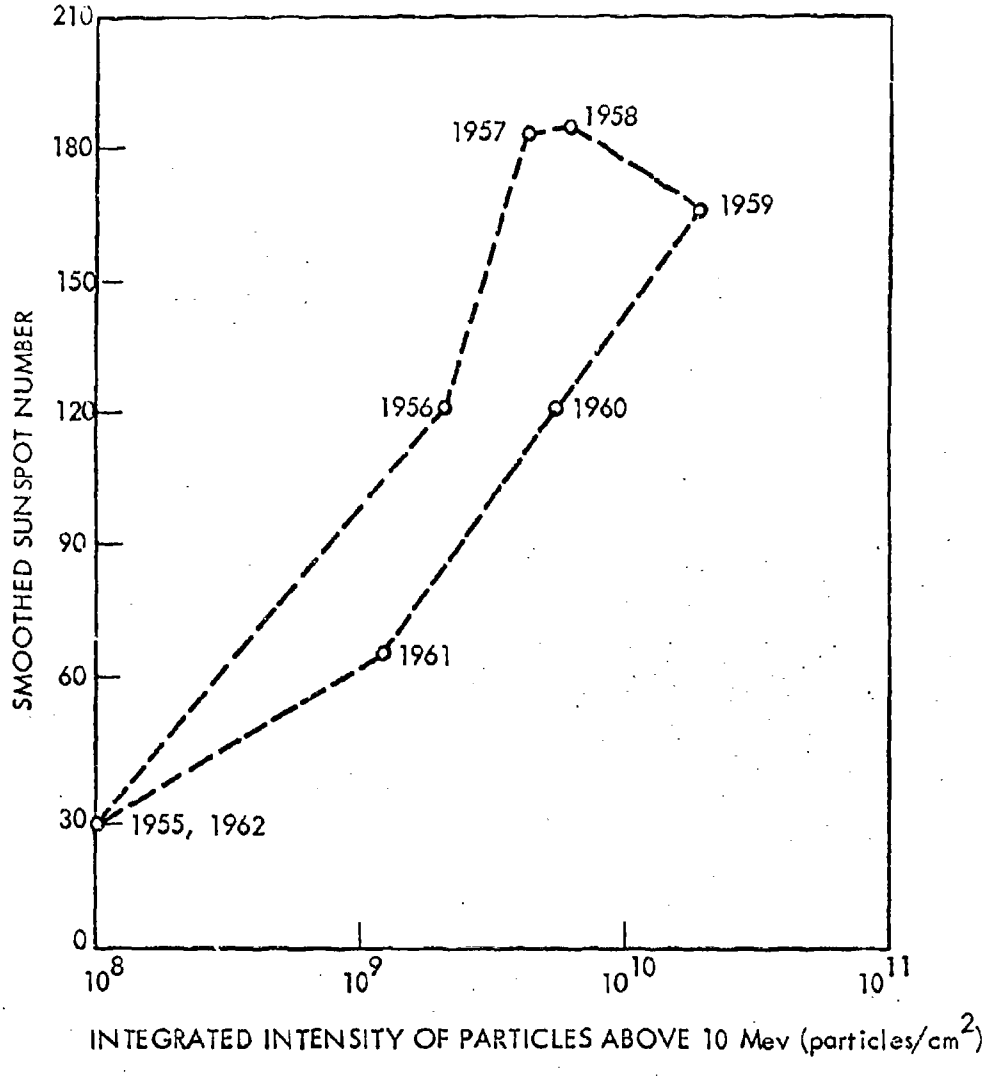

FIGURE 13. Smoothed sunspot number as a function of integrated intensity of solar cosmic rays above 10 Mev.

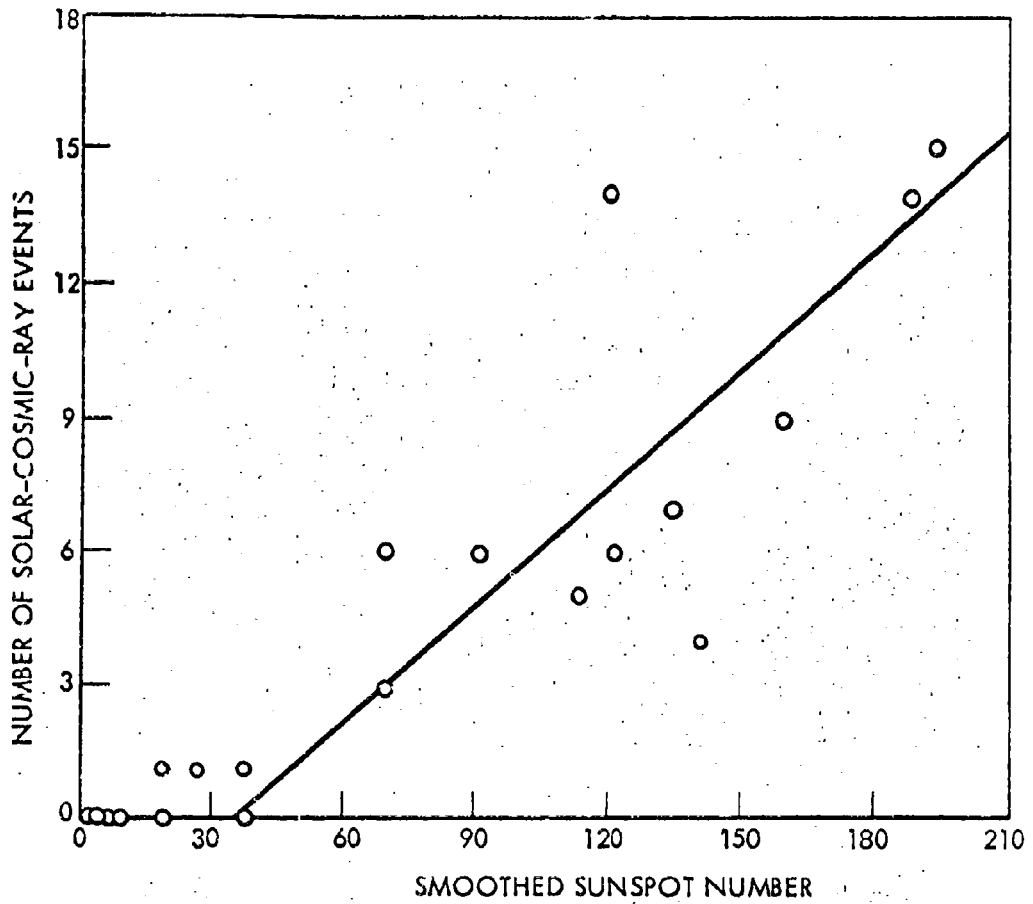

FIGURE 14. Number of solar-cosmic-ray events observed as a function of the smoothed sunspot number.

and space probes

As can be seen from Fig. 14, there is a usable degree of linear correlation between the two parameters. In particular, we see that during ten years when the yearly sunspot number has been less than forty, only three solar-cosmic-ray events have been observed--an average of 0.3 events/year. Further from Fig. 13, we see that the total yearly integrated intensity of particles above 10 Mev expected from these events is less than approximately $10^8/cm^2$, or approximately the integrated intensity of galactic cosmic rays in one year.

Observations over the past three sunspot minima show that the sunspot number remains below forty for an average of three years around each minimum. During the current period of sunspot minimum, which started early in 1962 and will probably extend to early in 1965, travel outside the earth's magnetosphere should be relatively safe.

The character of the next sunspot maximum is the subject of some study in the literature. According to the work of Gleissberg (Ref. 21), the next maximum will occur late in 1967 or early in 1968, and it will have a number of approximately 85. We recognize that the sunspot number of cycle 19 was the largest on record; in fact, the maximum sunspot number during cycle 18 was one of the largest on record. Thus, apparently 11-year cycles of high sunspot numbers are coming to an end in accordance

with the 80-year sunspot cycle. If we can extrapolate the correlations observed in cycles 18 and 19 to cycle 20 and accept Gleissberg's estimates of maximum sunspot number, In 1967 and 1968 we might expect five or six solar-cosmic-ray events per year and a yearly integrated inten.ity of particles above 10 Mev of about $10^9/cm^2$. Although the probability of obtaining events with flatter spectra appears greater due to the lower sunspot number, generally the hazard during the next period of sunspot maximum appears to be substantially reduced from the hazard during the previous maximum.

SOLAR-PARTICLE EVENT RADIATION DOSE DETERMINATION

Previous sections of this report have established that the principal radiation threat in the polar regions and the regions beyond the magnetosphere is the solar-particle event. In order to determine the magnitude of this threat for missions in these regions of space, it is necessary to calculate the radiation doses encountered within presently designed spacecraft. This section of the report is devoted to a description of the method used in calculating the radiation doses for solar-particle events.

In general, the method employed is that developed by D. L. Dye (Ref. 22). In this method, the unit flux dose or dose per proton is calculated by using a computer program. With this computer program, the unit flux dose may be determined at any point in any material for which a value of dE/dx is available. This material may be in free space or shielded by as many as twelve layers of different materials. In addition, the tissue depth dose may be determined by using a subroutine employing a body phantom. The unit flux dose includes primary protons and secondary radiations generated in the shielding materials and the body tissue. The radiation for the solar particle event is then determined by multiplying the unit flux dose times proton flux for the event.

The first step in calculating the unit flux dose is the specification of particle spectrum. From previous sections, it has been shown that the

radiation of the solar particle event is predominantly protons with energies from one Mev to a few Gev. The integral spectrum best describing the flux for a given event is:

$$J(>P) = J_o \exp(-\frac{P}{P_o}), \qquad \text{(Eq. 1)}$$

where P is the particle rigidity ($=\frac{\text{momentum}}{\text{charge}}$), and J(> P) is the number of particles of rigidity greater than P. The e-folding rigidity P_o varies from event to event, ranging from 50 to 200 Mv. In Table 6, the estimated integral flux at 10, 30, and 100 Mev is listed for those events for which sufficient data are available. For some events, only an estimate of the flux above 30 Mev can be made. In order to proceed, a value of P_o for these events must be determined. This is accomplished as follows. Substitution of

$$P = \frac{1}{q}\sqrt{T^2 + 2mT} \qquad \text{(Eq. 2)}$$

into Eq. 1, where T = kinetic energy, q = charge, and m = rest mass in energy units, gives the spectrum as a function of T, i. e.,

$$J'(>T) = J_o \exp\left[\frac{-1}{qP_o}\sqrt{T^2 + 2mT}\right]. \qquad \text{(Eq. 3)}$$

Substitution of T = 30 Mev and T = 100 Mev into Eq. 3 gives, for protons:

$$\frac{J'(>30)}{J'(>100)} = \exp\left[\frac{1}{P_o}\left(\sqrt{100^2 + 187600} - \sqrt{30^2 + 56280}\right)\right]. \qquad \text{(Eq. 4)}$$

TABLE 6. Integral Flux at 10, 30, and 100 Mev and Corresponding Characteristic Rigidity P_o

Date	J(> 10 Mev)	J(> 30 Mev)	J(> 100 Mev)	P_o
		(protons/cm^2)		(Mv)
2/23/56	1.8×10^9	1.0×10^9	3.5×10^8	195
3/11/56	-	-	-	-
8/ 3/56	-	2.5×10^7	6×10^6	144
11/13/56	-	-	-	-
1/20/57	-	2×10^8	7×10^6	61
4/ 3/57	-	-	-	-
6/22/57	-	-	-	-
7/ 3/57	-	2×10^7	-	-
8/ 9/57	-	1.5×10^6	-	-
8/29/57	-	1.2×10^8	3×10^6	56
9/21/57	-	1.5×10^6	-	-
10/20/57	-	5×10^7	1×10^7	127
11/ 4/57	-	9×10^6	-	-
2/ 9/58	-	1×10^7	-	-
3/23/58	2×10^9	2.5×10^8	1×10^7	64
4/10/58	-	5×10^6	-	-
7/ 7/58	1.8×10^9	2.5×10^8	9×10^6	62
8/16/58	4×10^8	4×10^7	1.6×10^6	64
8/22/58	8×10^8	7×10^7	1.8×10^6	56
8/26/58	1.5×10^9	1.1×10^8	2.0×10^6	51
9/22/58	9×10^7	6×10^6	1×10^5	50
5/10/59	5.5×10^9	9.6×10^8	8.5×10^7	84
6/13/59	-	8.5×10^7	-	-
7/10/59	4.5×10^9	1.0×10^9	1.4×10^8	104
7/14/59	7.5×10^9	1.3×10^9	1.0×10^8	80
7/16/59	3.3×10^9	9.1×10^8	1.3×10^8	105
8/18/59	-	1.8×10^6	-	-
1/11/60	-	4×10^5	-	-
4/ 1/60	1.5×10^7	5.0×10^6	8.5×10^5	116
4/ 5/60	-	1.1×10^6	-	-
4/28/60	1.3×10^7	5.0×10^6	7×10^5	104
4/29/60	-	7×10^6	-	-

TABLE 6. Integral Flux at 10, 30, and 100 Mev and Corresponding Characteristic Rigidity P_o (Cont'd)

Date	J(> 10 Mev)	J(> 30 Mev)	J(> 100 Mev)	P_o
		(protons/cm^2)		(Mv)
5/ 4/60	1.2×10^7	6×10^6	1.2×10^6	127
5/ 6/60	-	4×10^6	-	-
5/13/60	1.5×10^7	4×10^6	4.5×10^5	94
6/ 1/60	-	4×10^5	-	-
8/12/60	-	6×10^7	-	-
9/ 3/60	9×10^7	3.5×10^7	7×10^6	127
9/26/60	2×10^7	2.0×10^6	1.2×10^5	73
11/12/60	4×10^9	1.3×10^9	2.5×10^8	124
11/15/60	2.5×10^9	7.2×10^8	1.2×10^8	114
11/20/60	1.4×10^8	4.5×10^7	8×10^6	118
7/11/61	1.7×10^7	3×10^6	2.4×10^5	81
7/12/61	5×10^8	4×10^7	1×10^6	56
7/18/61	1×10^9	3×10^8	4×10^7	102
7/20/61	1.5×10^7	5×10^6	9×10^5	120
9/28/61	5×10^7	6×10^6	1.1×10^6	121
11/10/61	-	-	-	-
2/ 4/62	-	-	-	-
10/23/62	6×10^5	1.2×10^5	1×10^4	83

Solving Eq. 4 for P_o, we obtain

$$P_o = \frac{206}{\ln[J'(>30)/J'(>100)]} \text{ Mv}$$

The spectrum was fitted at the 30- and 100-Mev points rather than the 10 and 30 or 10 and 100 points because the protons below 30-Mev kinetic energy do not contribute appreciably to the dose for shielding thicknesses of a few gm/cm^2. The calculated values of P_o are listed in Table 6 for those events with two or more flux values. Thus, the unit flux dose for the i^{th} shielding configuration, d_i, is determined from Fig. 15 for the appropriate P_o. The radiation dose for each solar-particle event is then obtained by multiplying the unit flux dose and the integrated particle flux for that event.

The problem remains to determine a P_o for the thirteen remaining events having only one flux value. Since it is impossible to calculate the doses for these thirteen events, we must either associate a particular P_o with each event, based on some relationship of the observed P_o's to other quantities, or be content with arriving at the most probable or mean doses from the events. It is shown in Fig. 15 that the unit flux dose is a strong function of P_o for a given shielding configuration. This indicates that the use of an average P_o will not necessarily give the mean doses. It remains to be determined whether the P_o for a given event can be related to some other quantity. Variables to be considered include

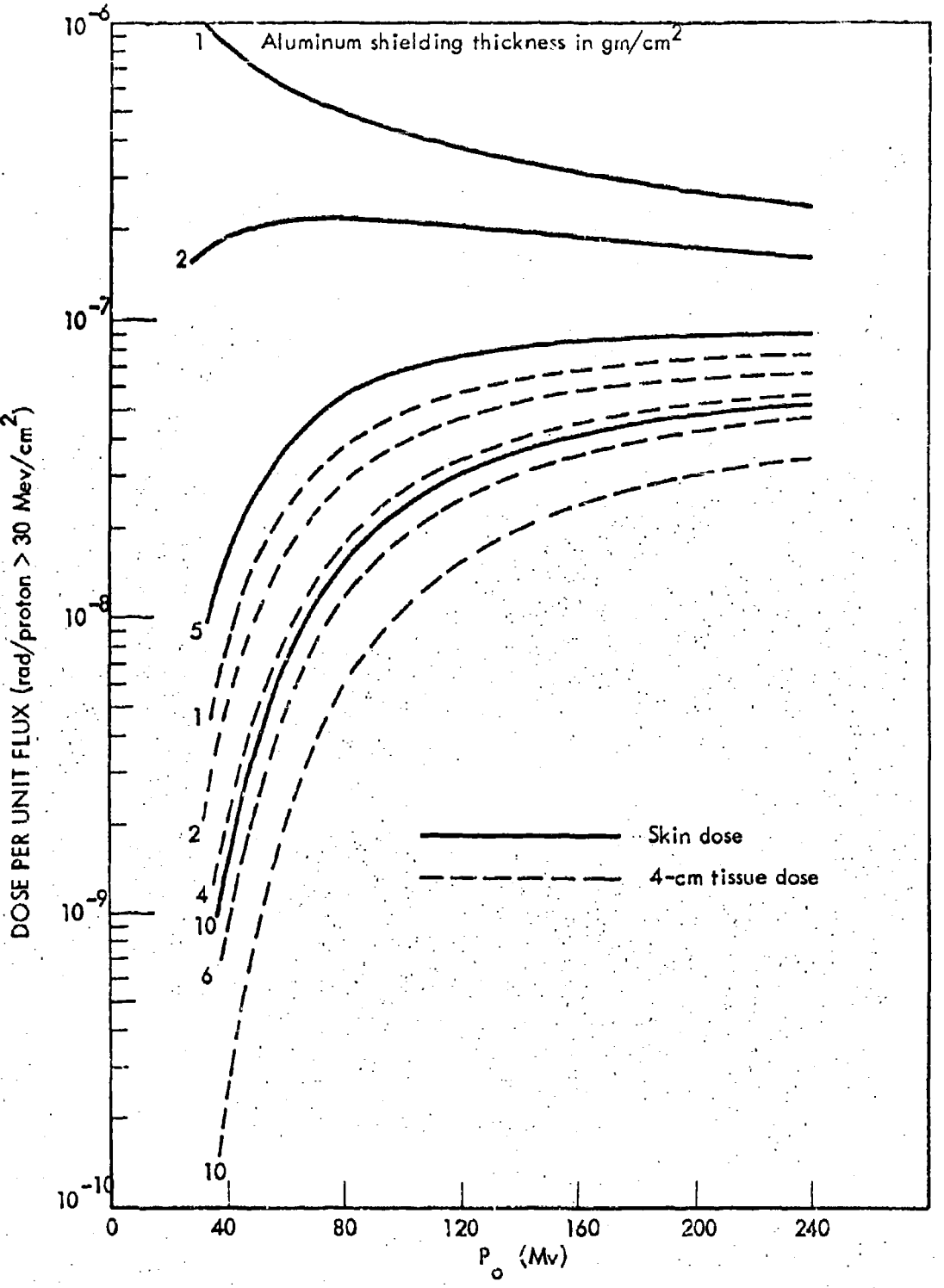

FIGURE 15. Dose calculations for exponential rigidity spectrum.

the total flux and the flare location on the sun's disk. Figure 16, a plot of the calculated P_o's versus the integrated flux above 30 Mev for the 31 events having two flux points, shows no apparent correlation between flux and P_o. In Figs. 17 and 18, the calculated P_o's are plotted as a function of the position of the solar flare producing the event on the sun's surface. Again, no correlation is apparent. From these figures, P_o is apparently a random quantity. To check this conclusion, the number of events having a P_o greater than a given rigidity P is plotted as a function of P in Fig. 19. Except for the single point having $P_o = 195$ for the February 23, 1956 event, the points fall roughly on a straight line. This graph supports the conclusion that the statistical distribution of P_o is rectangular between 45 and 150 Mv. We conclude, therefore, that df/dP_o, the probability density in P_o, is a constant, where

$$\frac{df}{dP_o} = \begin{cases} \frac{1}{150 - 45} & \text{for } 45 < P_o < 150 \text{ Mv}, \\ 0 & \text{for all other } P_o. \end{cases} \qquad \text{(Eq. 5)}$$

(Equation 5 can be deduced directly from Fig. 19 since it is essentially a plot of the cumulative probability versus P_o.)

The determination of the mean doses is now straightforward. If $d_i(P_o)$ is the unit flux dose as a function of P_o (Fig. 15) for the i^{th} shielding configuration and $\bar{d}_i$ is the mean of d_i, then

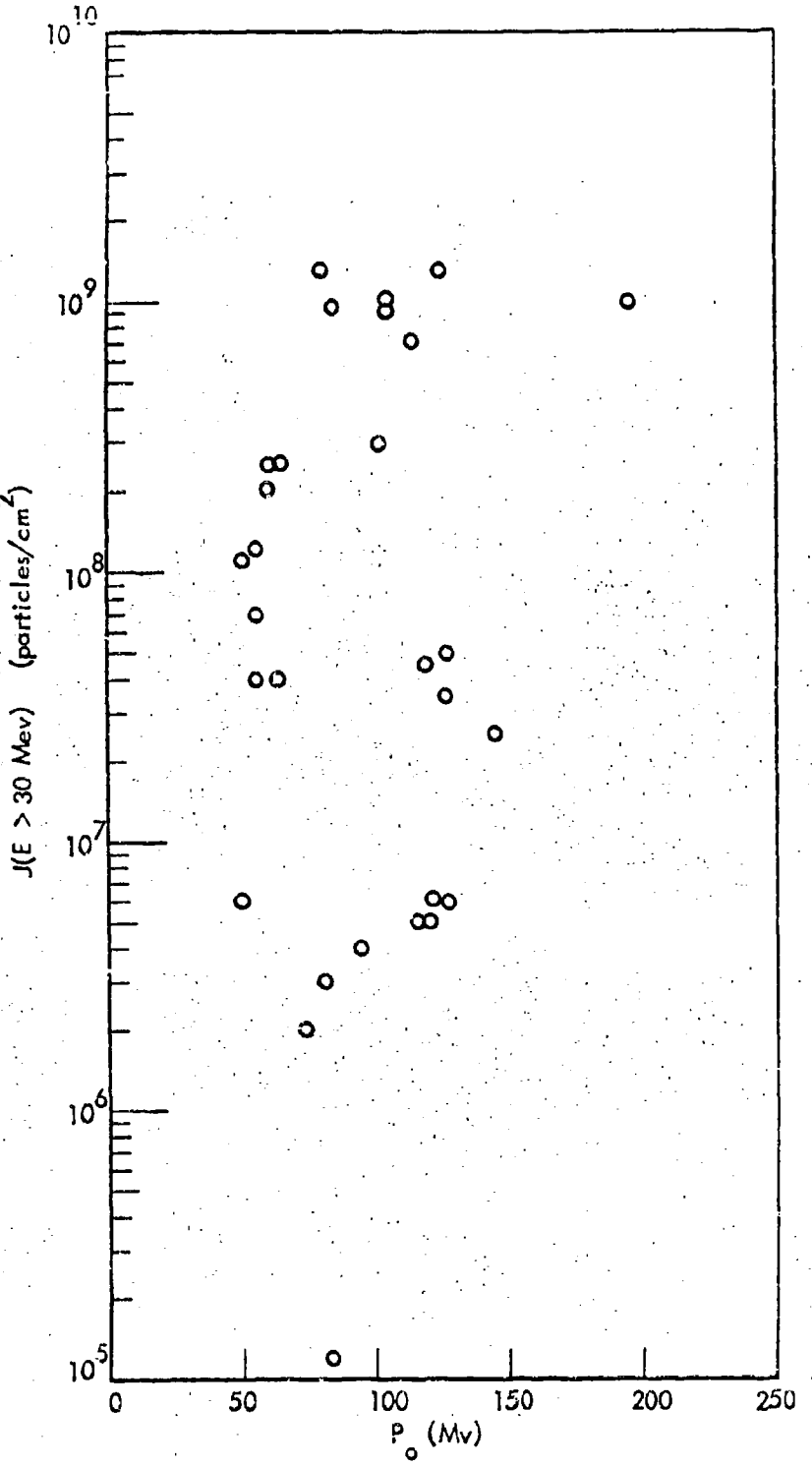

FIGURE 16. Plot of P_o versus integrated flux of particles above 30 Mev.

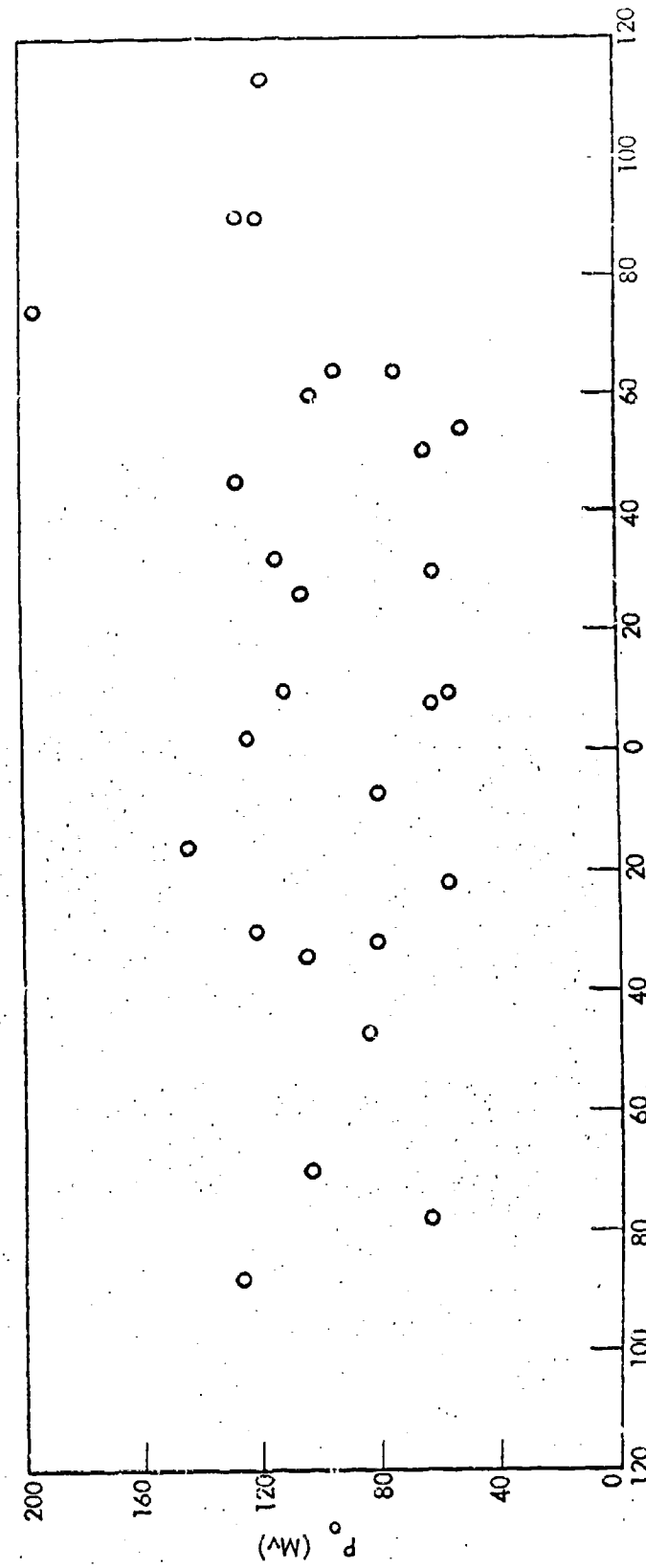

FIGURE 17. Plot of P_o versus longitude of the producing solar flare.

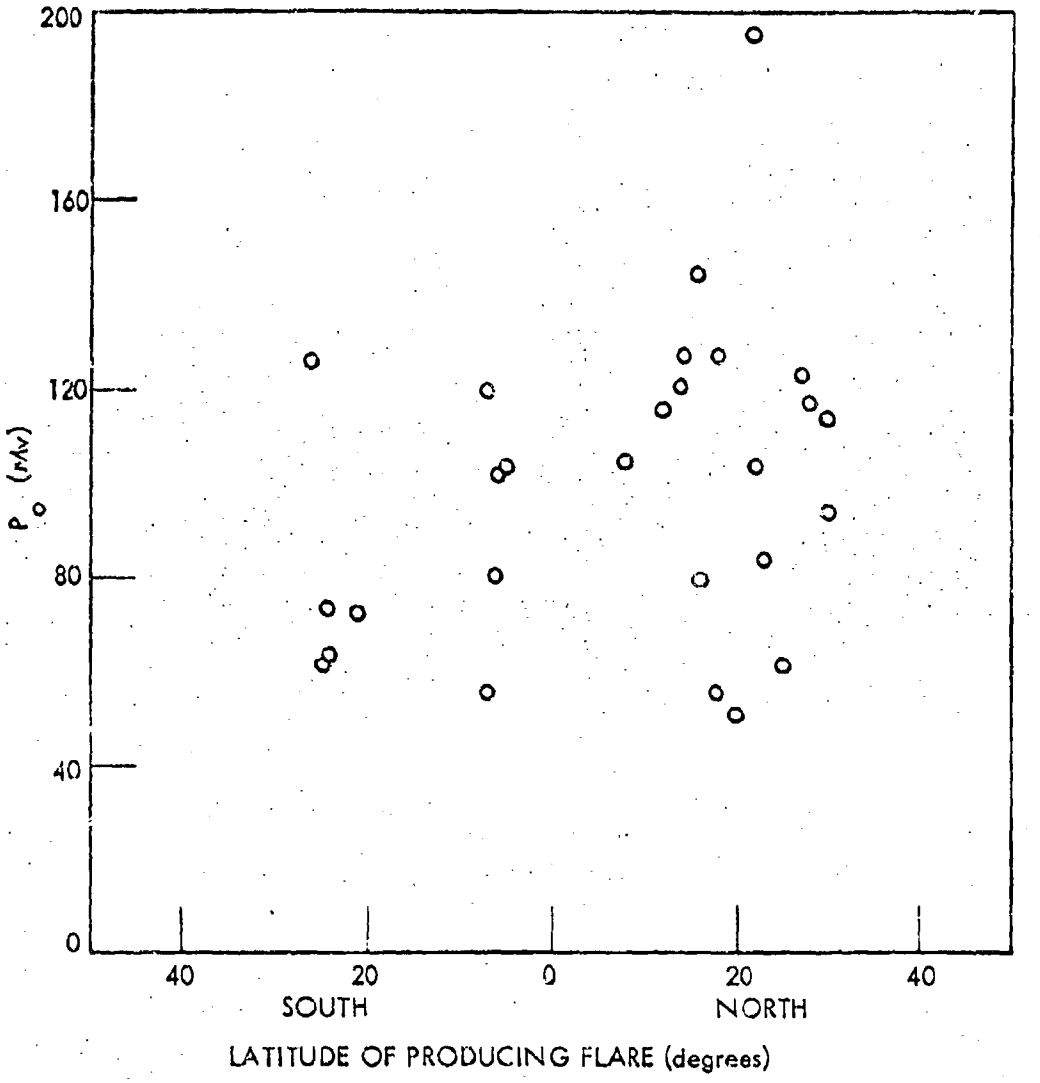

FIGURE 18. Plot of P_o versus latitude of producing solar flare.

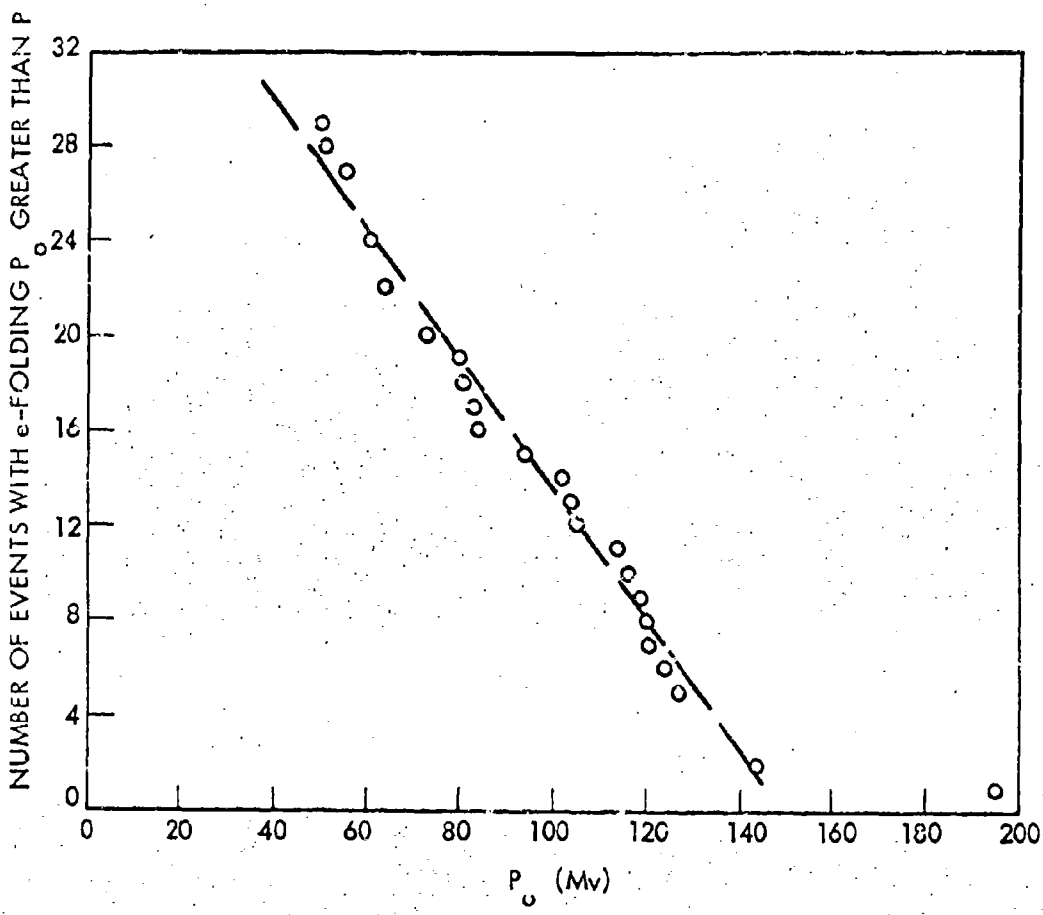

FIGURE 19. Integrated P_o distribution for solar-flare events.

$$\bar{d}_i = \int_{-\infty}^{\infty} \frac{df}{dP_o} d_i(P_o)\, dP_o$$

$$= \frac{1}{105} \int_{45}^{150} d_i(P_o)\, dP_o. \qquad \text{(Eq. 6)}$$

Thus, we need only integrate the curves in Fig. 15 to arrive at the various $\bar{d}_i$. Table 7 lists the values for $\bar{d}_i$ obtained in this manner. Table 8 (obtained by use of the calculated P_o when available and otherwise by use of Table 7) lists the doses by event for nine different shielding configurations.

The present computer shielding program can handle rather complicated shielding configurations. Figure 20 is an example of the manner in which a spacecraft is treated as a shielding configuration. The spacecraft is divided into an appropriate number of sectors and the number of grams per square centimeter is determined for each kind of material contained in that sector. This constitutes a shielding configuration designated by d_i. The existing program can handle up to 350 sectors and up to as many as twelve layers of different materials.

TABLE 7. Mean Unit Flux Dose $\bar{d}_i$ for Nine Shielding Configurations

Shielding Configuration*	$\bar{d}_i$**
	(rad/proton > 30 Mev)
10/4	9.89×10^{-9}
6/4	1.67×10^{-8}
4/4	2.35×10^{-8}
2/4	3.54×10^{-8}
1/4	4.32×10^{-8}
1/0	4.75×10^{-7}
2/0	2.08×10^{-7}
5/0	5.99×10^{-8}
10/0	$2/16 \times 10^{-8}$

* see Table 8

** see text

TABLE 8. Doses by Event for Nine Shielding Configurations

Date	Dose: Shielding Configuration 1/0*	2/0	5/0	10/0	1/4	2/4	4/4	6/4	10/4
	(rads)								
2/23/56	280	180	89	48	73	64	51	42.	30
3/11/56	-	-	-	-	-	-	-	-	-
8/ 3/56	8.5	5.0	2.0	0.93	1.60	1.35	1.03	0.78	0.53
11/13/56	-	-	-	-	-	-	-	-	-
1/20/57	122	42	7.2	1.40	4.6	3.2	1.76	1.02	0.42
4/ 3/57	-	-	-	-	-	-	-	-	-
6/22/57	-	-	-	-	-	-	-	-	-
7/ 3/57	9.5	4.2	1.2	0.43	0.86	0.70	0.47	0.33	0.20
8/ 9/57	0.71	0.31	0.09	0.03	0.06	0.05	0.04	0.03	0.01
8/29/57	77	25	3.8	0.65	2.3	1.56	0.82	0.47	0.18
9/21/57	0.71	0.31	0.09	0.03	0.06	0.05	0.04	0.03	0.01
10/20/57	18.5	10.0	3.9	1.65	3.0	2.5	1.80	1.35	0.85
11/ 4/57	4.3	1.87	0.54	0.19	0.39	0.22	0.21	0.15	[illegible]
2/ 9/58	4.8	2.08	0.60	0.22	0.43	0.35	0.24	0.17	0.10
3/23/58	148	54	10	2.10	6.4	4.5	2.55	1.53	0.66
4/10/58	2.4	1.04	0.30	0.11	0.22	0.18	0.12	0.08	0.05
7/ 7/58	150	54	9.5	1.93	6.0	4.3	2.35	1.40	0.59
8/16/58	23.7	8.6	1.60	0.34	1.02	0.72	0.41	0.24	0.11
8/22/58	45	14.7	2.24	0.38	1.33	0.91	0.49	0.27	0.11
8/26/58	75	22.3	3.0	0.43	1.76	1.17	0.57	0.30	0.11
9/22/58	4.1	1.22	0.16	0.02	0.10	0.06	0.03	0.02	0.01

TABLE 8. Doses by Event for Nine Shielding Configurations (Cont'd)

Date	Dose (rads)								
	Shielding Configuration								
	1/0*	2/0	5/0	10/0	1/4	2/4	4/4	6/4	10/4
5/10/59	470	206	55.	15.6	38.	29.3	18.2	12.5	6.4
6/13/59	40.	17.7	5.1	1.84	3.7	3.0	2.0	1.42	0.84
7/10/59	420	210	69	24.5	50	40	27.5	19.5	11.5
7/14/59	650	273	72	19.5	48	36.	22.8	15.1	7.5
7/16/59	382.	191.	63.	22.3	46.	36	25	17.7	10.5
8/18/59	0.86	0.37	0.11	0.04	0.08	0.06	0.04	0.03	0.02
1/11/60	0.19	0.08	0.02	0.01	0.02	0.01	0.01	0.01	0
4/ 1/60	1.95	1.05	0.37	0.15	0.28	0.23	0.16	0.12	0.07
4/ 5/60	0.52	0.23	0.07	0.02	0.05	0.04	0.03	0.02	0.01
4/28/60	2.1	1.05	0.35	0.12	0.25	0.20	0.14	0.10	0.06
4/29/60	3.3	1.46	0.42	0.15	0.30	0.24	0.16	0.12	0.07
5/ 4/60	2.2	1.20	0.47	0.20	0.36	0.30	0.22	0.16	0.10
5/ 6/60	1.90	0.83	0.24	0.09	0.17	0.14	0.09	0.07	0.04
5/13/60	1.80	0.85	0.26	0.08	0.18	0.14	0.09	0.07	0.04
6/ 1/60	0.19	0.08	0.02	0.01	0.02	0.01	0.01	0.01	0
8/12/60	0.22	0.12	0.05	0.02	0.04	0.03	0.01	0.01	0.01
9/ 3/60	13.0	7.0	2.73	1.16	2.10	1.75	1.26	0.95	0.60
9/26/60	1.08	0.43	0.10	0.02	0.06	0.05	0.03	0.02	0.01
11/12/60	484	263	100	43	75	62	46	34	20.8
11/15/60	288	151	53	20.5	39.6	31.7	23.0	16.6	10.1
11/20/60	17.3	9.4	3.4	1.35	2.52	2.07	1.49	1.08	0.68

TABLE 8. Doses by Event for Nine Shielding Configurations (Cont'd)

Date	Dose (rads)								
	Shielding Configuration								
	1/0*	2/0	5/0	10/0	1/4	2/4	4/4	6/4	10/4
7/11/61	1.47	0.64	0.17	0.05	0.12	0.09	0.06	0.04	0.02
7/12/61	25.7	8.4	1.28	0.22	0.76	0.52	0.28	0.15	0.06
7/18/61	128	63	20.4	7.2	15	12	8.1	5.7	3.3
7/20/61	1.90	1.03	0.38	0.15	0.29	0.23	0.17	0.12	0.08
9/28/61	2.28	1.24	0.46	0.18	0.35	0.28	0.20	0.14	0.10
11/10/61	-	-	-	-	-	-	-	-	-
2/ 4/62	-	-	-	-	-	-	-	-	-
10/23/62	0.06	0.03	0.01	0	0	0	0	0	0

* Shielding configurations are specified as I/J where I = shielding thickness in gm/cm^2 of aluminum, and J = tissue depth in cm.

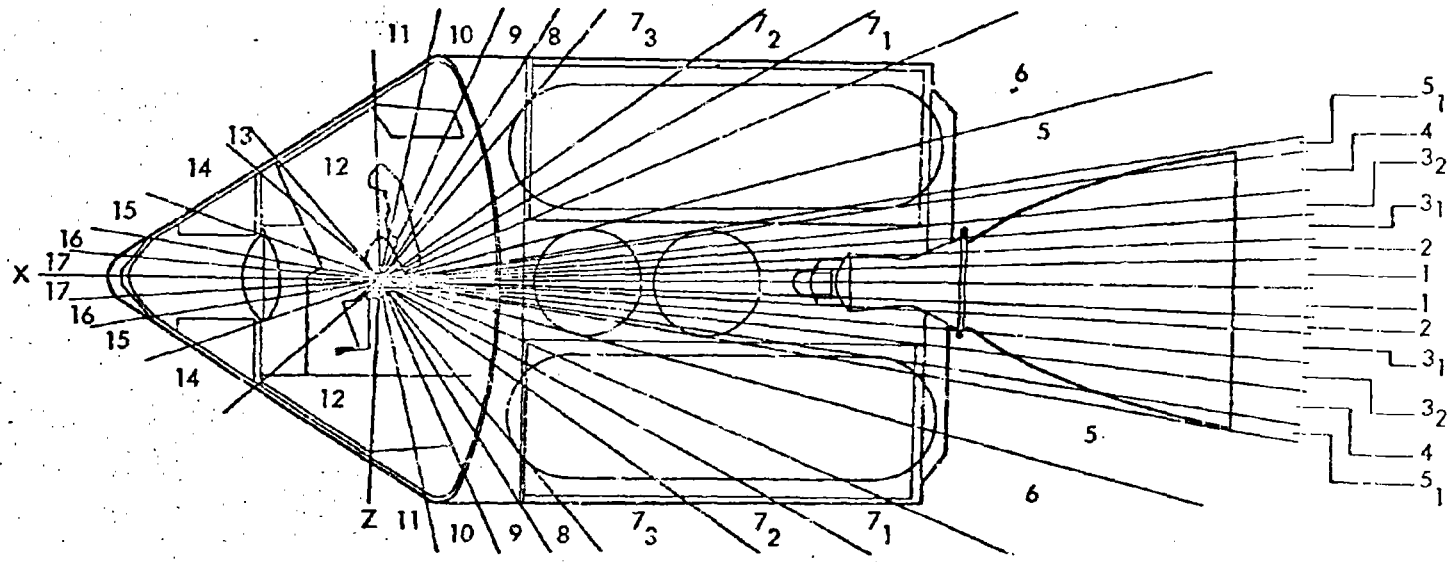

Side view of Apollo vehicle

FIGURE 20. Apollo space vehicle shielding thickness analysis.

GROSS RADIATION DOSE PREDICTION

Cumulative probability-dose curves for cycle 19 are constructed from Table 3 as follows. The mission, of duration T days, is considered to start on each consecutive day beginning January 1, 1956 and in each case the last mission ends on December 31, 1962. For each starting date, the dose which would have been received is recorded. After all the doses have been calculated, they are arranged in descending size. The number of mission intervals which sampled a dose larger than a given dose D may now be determined by numbering the descending doses consecutively. The probability of receiving a dose greater than D is then the ratio of this number to the total number of missions (2557 - T). (There are 2557 days from January 1, 1956 through December 31, 1962.)

Representative curves for mission durations of thirty and sixty days with shielding thicknesses of 1, 5, and 10 gm/cm^2 of aluminum are shown in Figs. 21 and 22. A program which carries out this portion of the calculation has been written for the IBM 7090. This program supplements the existing computer programs for calculating the doses and allows rapid construction of a probability-dose curve for any desired mission duration and shielding configuration.

In a similar fashion, cumulative probability-particle flux curves may be derived. Figure 23 gives the probability of receiving an integrated

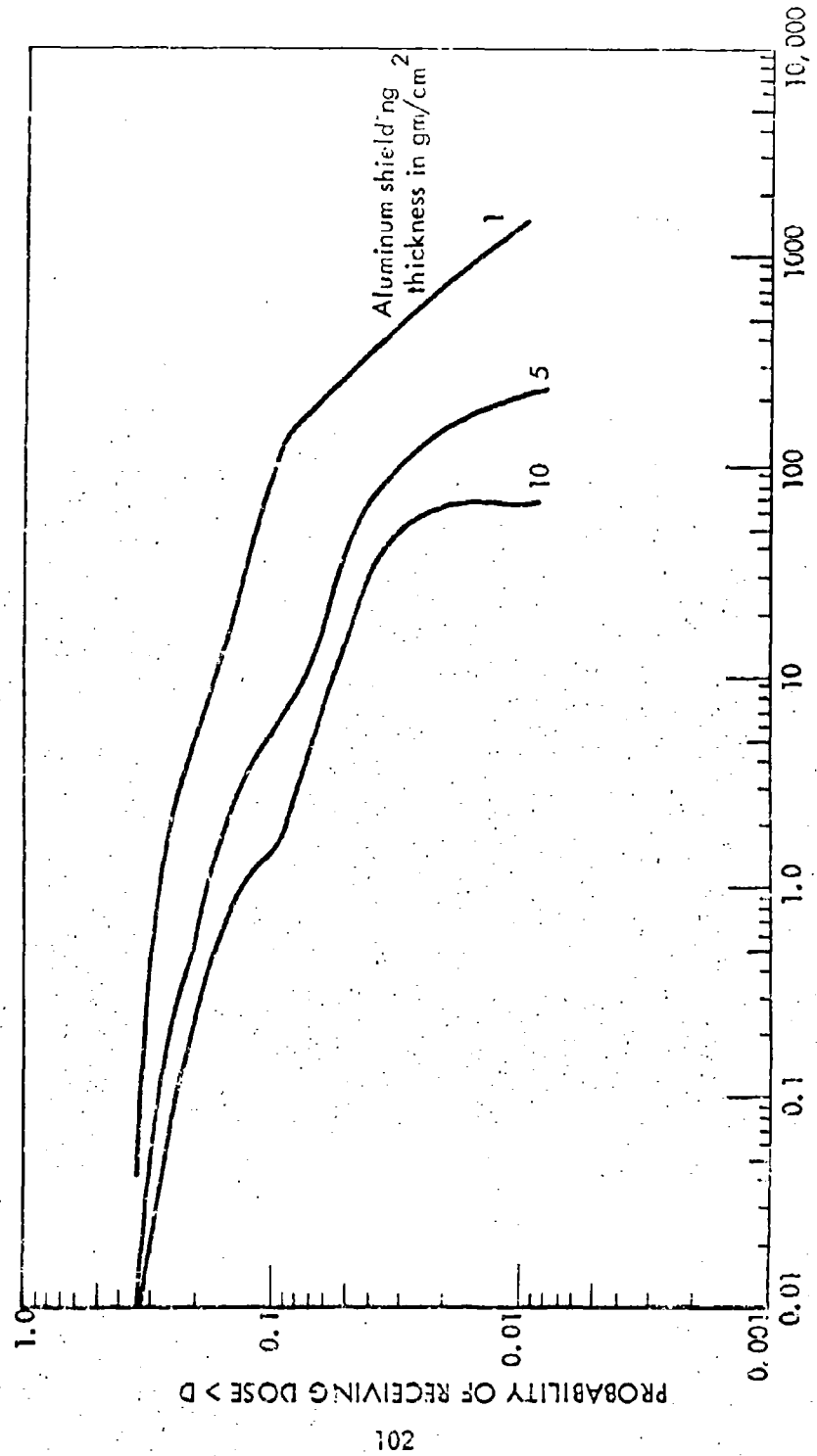

FIGURE 21. Cumulative probability-dose curves for 30-day mission.

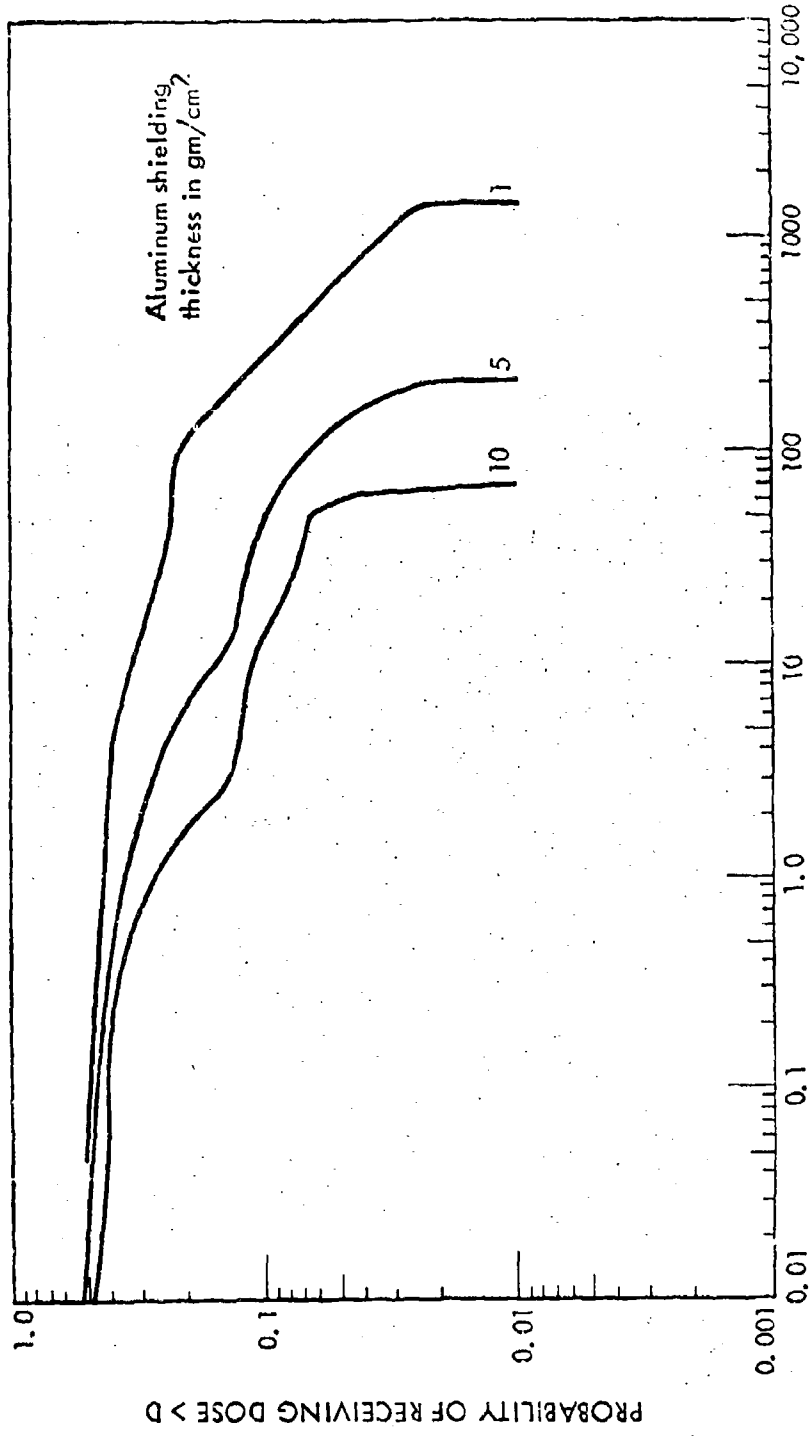

FIGURE 22. Cumulative probability-dose curves for 60-day mission.

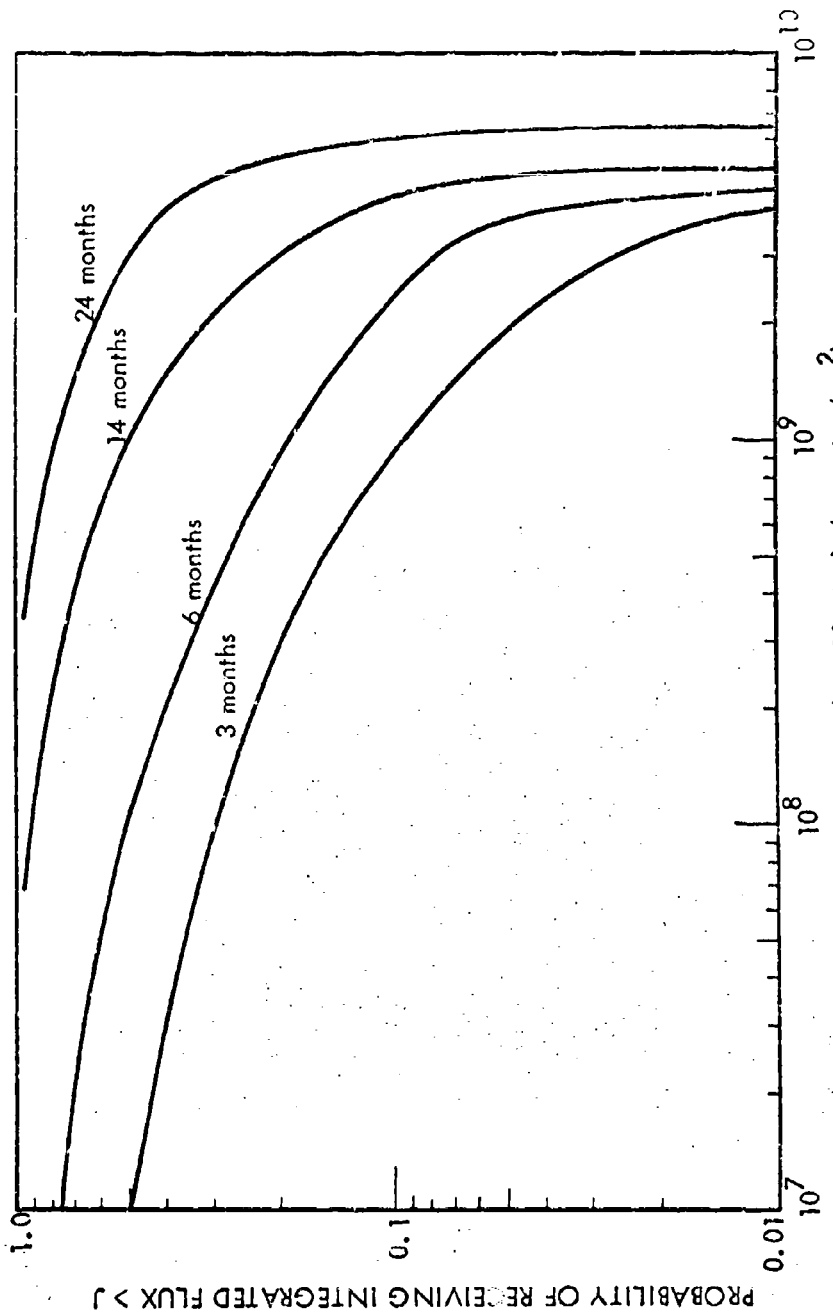

FIGURE 23. Cumulative probability–flux curves for various mission durations.

particle flux ($E > 30$ Mev) greater than a given integrated flux J for exposure times of 3, 6, 14, and 24 months.

The previous section of this report dealing with solar-particle event predictions indicates that the probability of encountering solar-flare-particle events can be substantially reduced by postponing scheduled missions or aborting missions in progress if certain solar conditions occur. The extent of the reduction and the approach to be employed will depend upon the mission type and mission duration.

Establishment of solar conditions to be used and calculations of the reduced probabilities for various missions is now under way in the Space Physics Group of The Boeing Company.

Some information concerning solar-particle events is summarized in Fig. 24, which is a plot of the smoothed sunspot numbers for solar cycles 18 and 19 with the maximum and minimum values predicted for solar cycle 20 (Refs. 21 and 23). The number of class 3 and 3+ flares per year and the number of particle events per year are also shown in this figure. The number of class 3 and 3+ flares for cycle 20 are predicted on the basis of correlations derived from cycles 18 and 19 (Ref. 24).

Examination of Fig. 24 indicates that the use of probability curves obtained for solar cycle 19 would apply to solar cycle 20 if solar activity reaches the maximum predicted. The dose probabilities obtained from

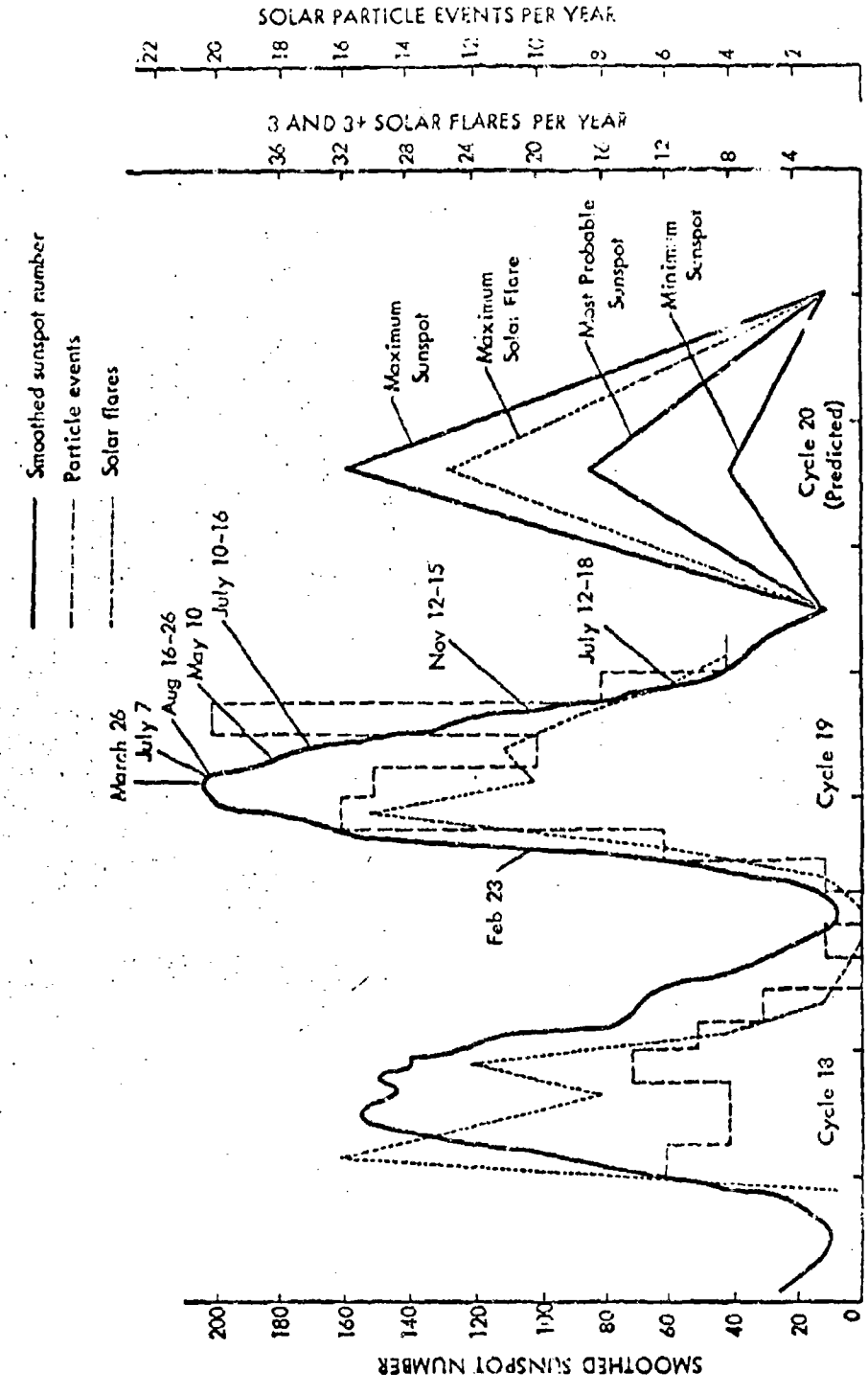

FIGURE 24. Solar activity.

such curves, then, would certainly be an upper limit for doses to be incurred during corresponding missions in cycle 20. Better predictions concerning the shape, the magnitude of the peak and time of peak of the smoothed sunspot curve, with corresponding changes in the predicted dose-probability curves, can be made after the beginning of solar cycle 20 (Ref. 21).

REFERENCES

1. H. Elliot, Progress in Cosmic Ray Physics, 1, 504, North Holland Publishing Co., Amsterdam (1952)

2. H. Carmichael, Space Science Reviews, 1, 28 (1962)

3. W. R. Webber, Progress in Cosmic Ray Physics, 6, 75, North Holland Publishing Co., Amsterdam (1962)

4. P. S. Freier and W. R. Webber, J. Geophys. Research, 68, 1605 (1963)

5. D. J. Hofmann and J. R. Winckler, J. Geophys. Research, 68, 2067 (1963)

6. K. G. McCracken, J. Geophys. Research, 67, 423, 435, 447 (1962)

7. P. S. Freier, J. Geophys. Research, 68, 1805 (1963)

8. S. Biswas, C. E. Fichtel, D. E. Guss, and C. J. Waddington, J. Geophys. Research, 68, 3109 (1963)

9. W. R. Webber and P. S. Freier, to be published

10. M. A. Ellison, S. M. P. McKenna, and J. H. Reid, Dunsink Observatory Publications, 1, No. 3

11. T. Takakura, Pub. Astronomical Soc. Japan, 12, 55 (1960)

12. W. A. Stein and E. P. Ney, J. Geophys. Research, 68, 65 (1963)

13. W. R. Webber, Can. J. Phys., 40, 906 (1962)

14. W. R. Webber, J. Geophys. Research, 67, 5091 (1962)

15. D. H. Jelly and C. Collins, Can. J. Phys., 40, 706 (1962)

16. D. K. Bailey and J. M. Harrington, Proc. International Conf. on Cosmic Rays II, Phys. Soc. Japan, 17, 334 (1962)

17. A. S. Beaprozvannaya, Proc. International Conf. on Cosmic Rays i, Phys. Soc. Japan, 17, 146 (1962)

18. C. G. Reed and H. Leinbach, J. Geophys. Research, 64, 1801 (1959)

19. W. C. Lin and J. A. Van Allen, Univ. of Iowa Report No. 15 (1963)

20. K. A. Anderson, NASA Technical Note D-700 (1961)

21. W. Gleissberg, Zeits fur Astrophysik 49, 25 (1960)

22. D. L. Dye and Gunning Butler, The Boeing Company, D2-10115, August 1961

23. C. W. Minnis, Nature, 186, 462 (1960)

24. V. B. Westburg, The Boeing Company, Memo 2-5412-10-RSG-5